Eur. J. Mech. B - Fluids 19 (2000) 423–452

S0997-7546(00)00120-5/FLA

Laminar mixed convection in a horizontal annular duct. Case of thermodependent non-Newtonian fluid

Chérif Nouar *, Braham Benaouda-Zouaoui, Christophe Desaubry

LEMTA-UMR 7563 (CNRS-INPL-UHP) ENSEM, 2 avenue de la Foret de Haye, BP 160, 54504 Vandoeuvre-lès-Nancy, France

(Received 10 May 1999; revised 30 November 1999, and 18 February 2000; accepted 21 February 2000)

Abstract – The experimental and numerical analysis of combined forced and free convection heat transfer of a non-Newtonian fluid in a horizontal annular duct is presented. The flow is laminar and Prandtl and Boussinesq hypotheses are adopted. The outer and inner cylinders are heated uniformly with a constant heat flux density. At the inlet of the annular duct, the flow is fully developed and the temperature profile is uniform. The governing equations are solved numerically using finite differences. The variation of the rheological properties with temperature is taken into account. Near the entrance, forced convection is the dominant mechanism. The core flow is decelerated because of the decrease of the consistency K as the temperature T increases near the heated walls. Simultaneously, the downstream flow between the two cylinders caused by the displacement of the secondary boundary layer induces an acceleration of the flow in the lower part of the annular duct and a deceleration in the upper part. Further downstream, the fluid warms up and the buoyancy force effect becomes strong enough to overcome the forced flow. The critical Cameron number X_c^+, above which the convection mechanism becomes dominated by natural convection is determined using scaling analysis. The results are found to agree well with the numerical solution. For $X^+ < X_c^+$ and for a large Péclet number, an asymptotic solution is obtained by perturbing the forced convection solution. However, far from the entrance region, the thermal stratification induced by buoyancy force combined with the variation of K with T lead to another flow reorganization. There is an acceleration of the flow in the upper half part of the annular duct and a deceleration in the lower half one. © 2000 Éditions scientifiques et médicales Elsevier SAS

mixed convection / annular duct / non-Newtonian / variable consistency

1. Introduction

Many fluids of interest in industrial practice exhibit non-Newtonian fluid behavior. Extensive research has been undertaken over the last three decades, which has largely focused on engineering analysis, such as the design of heat exchangers for non-Newtonian fluids. This requires the knowledge of the dynamic flow behavior and the temperature distribution field, which depend on the dynamical conditions, geometry, rheological behavior and on the variation of the rheological parameters with temperature. In many practical situations, the fluid density variation with temperature has to be taken into account, making it necessary to incorporate buoyancy force effects in the flow analysis. In the case of horizontal geometry, natural convection induces a thermal stratification in the vertical cross section and improves the heat transfer rate. Mixed convection heat transfer for Newtonian fluid in horizontal duct has been studied quite extensively since the early work of Morton [1]. The case of annular duct was also investigated by several authors; see for instance, and to name a few, Mojtabi and Caltagirone [2], Kotake and Hattori [3], Terhmina et al. [4], Nonino and Del Giudice [5]. The four kinds of boundary conditions described by Lundbeg et al. [6] were considered. In most of these studies and in others not explicitly cited, the fluid is assumed Newtonian and the effect of variation of the viscosity with temperature is neglected. In addition, to our knowledge, no attention has been paid in the past to the situation

* Correspondence and reprints; e-mail: cnouar@ensem.u-nancy.fr

where the two cylinders are heated at a constant heat flux density, Φ, despite its relevancy in many industrial problems. This boundary condition type is more suitable for the design of heat exchangers for the food industry.

When the fluid enters the annular duct, a thermal boundary layer develops on the walls of the cylinders. Due to the decrease of the fluid consistency K with temperature T, the fluid is accelerated near the heated wall and decelerated in the central part of the annular duct for flow rate conservation. This motion generates node-like sinks along the walls of the annular duct and causes fluid particles to move towards the wall. Simultaneously, the fluid near the heated wall is warmer, and therefore lighter, than the fluid removed from the wall; it therefore flows upward along the wall, and continuity requires a downflow of the heavier fluid between the two cylinders. As a result, there is a secondary flow motion, which can be viewed as two counter-rotating cells. The downstream flow between the two cylinders induces an acceleration of the flow in the lower part of the annular duct and a deceleration in the upper part. Near the entrance section, the forced convection is the dominant mechanism. The effect of the radial motion of fluid particles from the core flow to the heated walls decreases along the heating zone. On the other hand, the buoyancy force effect increases along the heating zone. For a critical axial position X_c^+, the two mechanisms are of the same order. From X_c^+, the buoyancy force effect becomes dominant. The upward movement of the warmer fluid and downward movement of the colder fluid lead progressively to the appearance of a low density fluid layer with a higher temperature at the upper part of the annular duct. This thermal stratification, combined with the decrease of K as T increases, induces another flow reorganization.

In the present work, an analysis of the laminar flow of non-Newtonian fluids under the influence of both forced and free convection is presented. The flow rate through the annular duct is imposed. The programme of work has two objectives, namely (a) to determine the effect of the rheological behavior of the fluid and the variation of K with T on X_c^+, on the intensity of recirculation and on the thermal stratification; (b) to add to the store of basic knowledge of heat transfer in the internal mixed convection for non-Newtonian fluids. The governing equations are solved numerically using a finite difference technique. The interaction of the two convective mechanisms is analyzed in details in terms of the drag coefficient and heat transfer rates. In order to distinguish the effects of thermodependent consistency from that of free convection and of rheological behavior on the flow dynamic and temperature profiles, three situations are considered. Firstly, forced convection coupled with thermodependent consistency is analyzed. Secondly, we consider the problem of mixed convection with constant rheological properties. Finally, having examined independently the effect of the variation of the rheological properties and that of the buoyancy force on the flow structure, the problem of mixed convection with variable consistency is analyzed.

This paper is organized as follows. The experimental installation, instrumentation and test fluids are described in section 2. The governing equations under the usual Boussinesq assumption are stated in section 3. The numerical solutions are obtained using finite differences. The discretization scheme and the algorithm used are outlined in section 4. An asymptotic solution is presented in section 5. The results concerning the flow and the temperature distribution are given and analyzed in section 6. Finally, conclusions on the main findings of the present analysis are drawn in section 7.

2. Experimental study

2.1. Apparatus

The test cell consists of two stainless steel coaxial cylinders. The inner and outer cylinders are 3.0 m long with outside diameters of 25.4 mm and 61.9 mm and wall thicknesses of 1.65 mm and 1.6 mm, respectively. An annular duct, 3.0 m long with an aspect ratio of 0.421 is thus built. It is extended at each end by a 15 cm

long of Plexiglass annular duct of the same cross section. This allows the establishment of the flow regime at the entrance of the heating zone and the LDV measurement of the axial velocity at the exit of the heating zone. According to Tiu and Bhattacharya [7], a distance of 15 cm is sufficient for the development of the dynamical regime for all the experimental tests.

The two cylinders of the test cell are heated by passing an electrical current through the tube wall. Nine stainless-steel fins have been soldered onto the tubes at three different axial positions (3×3), (at the entry, in the middle, at the exit of the test cell) to insure the coaxiality of the two cylinders and to allow the electric current to flow from the outer cylinder to the inner one. The electrical resistivity, ρ_{elec}, of the stainless steel (316 L) varies with temperature as: $\rho_{elec} = 7.4 \cdot 10^{-7}[1 + 85 \cdot 10^{-5}(T - 20)]$ Ω.m. When the wall temperature increases from 20°C to 80°C, ρ_{elec} increases by 5%. For all the experimental tests, ρ_{elec} is calculated at the mean wall temperature. The electrical power was provided to the outer cylinder by a self transformator of the voltage. The voltage at each cylinder varies from 1 to 10 V. The electrical current intensity passing in the ducts exceeds 1000 A. The voltage drop over the cylinders is measured by a digital voltmeter with an accuracy of ±0.01 V. The evolution of the outer cylinder wall temperature is determined by means of thirty thermocouples placed at thirteen different axial positions. Two thermocouples per section, one at the top and the other at the bottom, at the first eleven axial positions and four thermocouples placed 90° apart for the two last sections. All the thermocouples are of Chromel-Alumel type. The axial position of the thermocouples was chosen on the basis of Lévêque solution, $(T - T_e) \propto x^{1/3}$, such that the temperature measurements are uniformly distributed on the curve giving $\log(T)$ versus $\log(x^*)$. The fluid temperature T_e at the inlet of the heated test section, was also measured by a chromel-Alumel thermocouple and maintained constant, within tolerance of 0.1°C, during each experimental test. The test section is covered by a 10 cm thick polyurethane foam to minimize the heat exchange with the environment.

2.2. Instrumentation and control

The flow rate Qv, is measured by an electromagnetic flowmeter (PICOMAG-DMI 6530). The pressure drop between the inlet and the outlet sections, is measured by a differential pressure transducer, powered by a 5 V source with an accuracy of 1%.

The velocity measurements are performed using a Laser Doppler Velocity system from DISA. It comprises a 35 mW helium–neon laser and a focusing lens to form the control volume in the test section. The principal characteristics of the optical system are given in *table I*. The light scattered by particles, passing through this volume, is collected in the photomultiplier and processed by a Doppler frequency tracker. The axial velocity profiles were measured at 4.5 cm from the end of the heating zone and for three azimuthal positions: along a horizontal radius, vertical radius from the top and vertical radius from the bottom. The maximum error on the beam crossing position is of 0.25 mm.

Table I. Characteristics of the optical arrangement.

Focal length of the focusing lens (mm)	120
Half angle of the beam interaction (degrees)	10.62
Fringe spacing (μm)	1.73
Diameter of the control volume at $1/e^2$ intensity in air (μm)	90
Length of the control volume at $1/e^2$ intensity in air (μm)	500
Frequency to velocity conversion (ms^{-1}/MHz)	1.7168
Number of fringes	52

2.3. Fluids used

The fluids used were dilute aqueous solutions of the following polymers: (i) sodium carboxymethylcellulose (CMC) supplied by PROLABO: 1% and 2% weight concentration CMC solutions were used and (ii) CMC7M1C supplied by PROLABO, 2% weight concentration. They are prepared by dissolving the polymer powder in demineralized water. A small amount of preservative (formaldehyde) was added in order to limit bacterial contamination. These fluids are chosen because they are: (i) shear thinning; (ii) optically transparent and (iii) relatively stable with respect to thermal and mechanical treatments.

The cone and plate geometry of a Carrimed (CS-100) constant torque rheometer was used in order to study the rheological behavior of the working fluid. The rheograms were determined at different temperatures ranging from 10°C to 60°C. The curves fitted indicate that the rheological behavior of the solutions (i) and (iii) can be described by the Oswald–de Waele power law model: $\tau = K\dot{\gamma}^n$, in the range of shear rates, $\dot{\gamma}$, from 0.7 to about 400 s^{-1}. The rheological parameters have been determined in the range of shear rate that offers the best correlation coefficient (≈ 0.999).

It appears that the temperature dependence of n is weak compared to the temperature dependence of K. The relation $K - T$ adopted is $K = a\exp(-bT)$. One has to note that the polymer solutions deteriorate gradually with time because of the thermal and mechanical constraints that they undergo in the experimental device. Therefore, the rheological behavior of the working fluid was determined after each experimental test. The rheological parameters of the working fluids just after preparation are given by:

1% CMC: $\tau = 0.1\exp(-0.031T)\dot{\gamma}^{0.90}$,

2% CMC: $\tau = 0.84\exp(-0.038T)\dot{\gamma}^{0.83}$,

1% CMC7M1C: $\tau = 0.024\exp(-0.0245T)\dot{\gamma}$: Newtonian solution.

The thermal conductivity λ and the specific heat Cp are assumed to be that of the water solvent since the polymer concentration is very low.

2.4. Range of tests covered

For all the experimental tests, the variation range of the working conditions is: 500 (l/h) $\leqslant Qv \leqslant$ 1330 (l/h) and 2000 $W/m^2 \leqslant \Phi \leqslant 8500\ W/m^2$. The corresponding variations of the dimensionless numbers (defined is section 3) are: $200 \leqslant Pr \leqslant 1520$, $18 \leqslant Re \leqslant 131$, $233 \leqslant Gr \leqslant 22350$ and $4 \leqslant Pn \leqslant 16$.

3. Governing equations

The inner and outer cylinders of radii R_1 and R_2, respectively, are subjected to a constant heat flux density Φ. At the entrance of the heated region ($x^* = 0$), the flow is fully developed and the fluid temperature is constant and uniform. The coordinate system, (r^*, ϕ, x^*) the radial v^*, azimuthal w^*, and axial u^*, velocity components are shown in *figure 1*. The mathematical formulation is written on the basis of the following assumptions: (i) the fluid is incompressible and the flow is steady, (ii) the Péclet number Pe is sufficiently large [8] ($Pe \geqslant 100$) so that, momentum and heat diffusion in the axial direction can be neglected; (iii) the Brinkman number is too small, to neglect the viscous dissipation effect; (iv) the fluid density variation due to heating, $\rho - \rho_r = -\rho_r\beta(T - T_r)$, is considered important only in the buoyancy term. This is known as the Boussinesq approximation. Here, β is the thermal expansion coefficient and T_r is a reference temperature, taken as the mean temperature over the cross section; (v) the variation of the axial pressure gradient at a cross-plane is small while considering the axial momentum equation. As a consequence of the latter assumption, the

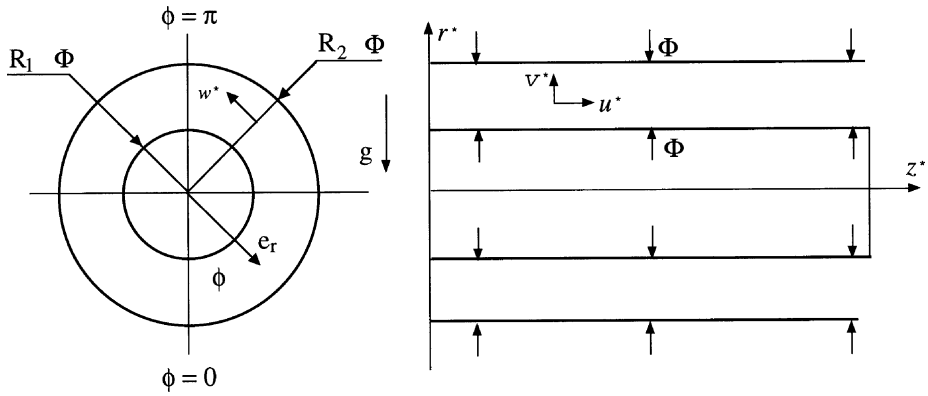

Figure 1. Geometry and coordinates system.

pressure can be decomposed as: $\tilde{p} = p_m(x^*) + p'(r^*, \phi)$. Here, $\tilde{p}$ is the pressure deviation $(p - p_0)$ from the hydrostatic value defined by: $\nabla p_0 = \rho_m \mathbf{g}$ where, $\mathbf{g}$ is the gravitational acceleration vector. The pressure p_m can be appropriately viewed as a space-averaged pressure over a cross section. The principal drawback of this model is that it does not allow for flow recirculation in the axial direction.

Remark: Following the methodology of D.D. Gray and A. Giorgini [9], it can be shown that the condition under which the Boussinesq approximation applies, is given by: $\beta \Phi R_2/\lambda \leqslant 0.1$. For our experimental conditions, this corresponds to $\Phi \leqslant 8800\ W/\mathrm{m}^2$.

The dimensionless governing equations of the problem are written in cylindrical coordinates. They are stated as follows.

3.1. Continuity equation

$$\nabla.\mathbf{V} = 0. \tag{1}$$

3.2. Radial momentum equation

$$\begin{aligned}
&\frac{1}{Pr(1-r_1)^2}\left[(\mathbf{V}.\nabla)V - \frac{W^2}{r}\right] \\
&\quad = -\frac{\partial P'}{\partial r} - GrPr(1-r_1)^2\Theta\cos\phi + \bar{\mu}_a\left[\Delta V - \frac{V}{r^2} - \frac{2}{r^2}\frac{\partial W}{\partial \phi}\right] + 2\frac{\partial \bar{\mu}_a}{\partial r}\frac{\partial V}{\partial r} + \frac{\partial \bar{\mu}_a}{\partial X}\frac{\partial U}{\partial r} \\
&\qquad + \frac{1}{r}\frac{\partial \bar{\mu}_a}{\partial \phi}\left[\frac{\partial W}{\partial r} + \frac{1}{r}\frac{\partial V}{\partial \phi} - \frac{W}{r}\right] + \mathrm{O}\left(\frac{1}{Pe^2}\right).
\end{aligned} \tag{2}$$

3.3. Tangential momentum equation

$$\frac{1}{Pr(1-r_1)^2}\left[(\mathbf{V}.\nabla)W+\frac{VW}{r}\right]$$
$$=-\frac{1}{r}\frac{\partial P'}{\partial\phi}+GrPr(1-r_1)^2\Theta\sin\phi+\bar{\mu}_a\left[\Delta W-\frac{W}{r^2}+\frac{2}{r^2}\frac{\partial V}{\partial\phi}\right]+\frac{\partial\bar{\mu}_a}{\partial r}\left[\frac{\partial W}{\partial r}-\frac{W}{r}+\frac{1}{r}\frac{\partial V}{\partial\phi}\right]$$
$$+\frac{2}{r}\frac{\partial\bar{\mu}_a}{\partial\phi}\left[\frac{V}{r}+\frac{1}{r}\frac{\partial W}{\partial\phi}\right]+\frac{\partial\bar{\mu}_a}{\partial X}\frac{1}{r}\frac{\partial U}{\partial\phi}+\mathrm{O}\left(\frac{1}{Pe^2}\right). \tag{3}$$

3.4. Axial momentum equation

$$\frac{1}{Pr(1-r_1)^2}[\mathbf{V}.\nabla]U=-\frac{\mathrm{d}P_m}{\mathrm{d}X}+\bar{\mu}_a\Delta U+\left[\frac{\partial\bar{\mu}_a}{\partial r}\frac{\partial U}{\partial r}+\frac{1}{r^2}\frac{\partial\bar{\mu}_a}{\partial\phi}\frac{\partial U}{\partial\phi}\right]+\mathrm{O}\left(\frac{1}{Pe^2}\right). \tag{4}$$

3.5. Continuity equation in integral form

$$\int_0^{\pi}\int_{r_1}^{1}rU\,\mathrm{d}r\,\mathrm{d}\phi=\frac{\pi}{2}\left[1-r_1^2\right]. \tag{5}$$

3.6. Energy equation

$$[\mathbf{V}.\nabla]\Theta=(1-r_1)^2\Delta\Theta+\mathrm{O}\left(\frac{1}{Pe^2},Br\right), \tag{6}$$

where

$$\mathbf{V}=\left[V,W,U\right]^t;\qquad\Delta=\left[\frac{\partial^2}{\partial r^2}+\frac{1}{r}\frac{\partial}{\partial r}+\frac{1}{r^2}\frac{\partial^2}{\partial\phi^2}\right]\quad\text{and}\quad[\mathbf{V}.\nabla]=\left[U\frac{\partial}{\partial X}+V\frac{\partial}{\partial r}+\frac{W}{r}\frac{\partial}{\partial\phi}\right].$$

In equations (4)–(6), *Pr*, *Gr*, *Br* and *Pe* are respectively the Prandtl, Grashof, Brinkman and Péclet numbers. They are defined by:

$$Pr=\frac{\mu_0 Cp}{\lambda};\qquad Gr=\frac{{\rho_e}^2 g\beta\langle\Delta T\rangle{R_2}^3}{{\mu_0}^2};\qquad Br=\frac{\mu_0 U_d^2(1-r_1)^2}{\Phi R_2};\qquad Pe=\rho_e CpU_dR_2/\lambda,$$

with $\langle\Delta T\rangle=\Phi R_2/\lambda$ and $r_1=R_1/R_2$.

The above equations are rendered dimensionless by using the following scales [10]:

$$U=\frac{u^*}{U_d};\qquad r=\frac{r^*}{R_2};\qquad X=\frac{x^*}{L};\qquad V=\frac{v^*L}{R_2U_d};\qquad W=\frac{w^*L}{R_2U_d};\qquad\bar{\mu}_a=\frac{\mu_a}{\mu_0}, \tag{7}$$
$$\Theta=\frac{(T-T_e)\lambda}{\Phi R_2};\qquad P_m=\frac{p_m{R_2}^2}{\mu_0U_dL};\qquad P'=\frac{p'L}{\mu_0U_d}.$$

μ_a is the apparent viscosity of the fluid calculated at the local temperature T, μ_0 corresponds to the apparent viscosity calculated at the inlet temperature T_e, and at the outer cylinder wall shear rate, for fully developed Poiseuille flow, U_d is the mean axial velocity, L is a typical axial scale length of temperature variations. It is given by: $L = \rho_e C p U_d (R_2 - R_1)^2/\lambda$. It can be viewed as a length over which, downstream convection balances transverse conduction: $L/R_2(1 - r_1)^2 = Pe$. The reference scales for the radial and azimuthal velocities are determined from the continuity equation. This change of variables was adopted in order to have dimensionless variables of order 1.

In the present study, it is assumed that the rheological behavior of the fluid is described by the power law model

$$\tau = 2\mu_a \mathbf{D}, \tag{8}$$

where τ and $\mathbf{D}$ are the deviatoric extra-stress, and deformation rate tensors. The apparent viscosity μ_a is given by:

$$\mu_a = K\left(4D_{II}\right)^{(n-1)/2}, \tag{9}$$

where K is the consistency parameter, n is the behavior index and the scalar D_{II} is the second invariant of tensor $\mathbf{D}$. In this study, we assume that n is temperature independent and K varies with temperature as $K = a\exp(-bT)$. A singularity in (9) occurs as $D_{II} \to 0$. To overcome this difficulty, a modified version of the rheological equation is used. When the value of D_{II} is less than a critical value $D_{II,c}$, the apparent viscosity is 'frozen' at a value calculated with $D_{II,c}$. This method was adopted by several authors. The value of $D_{II,c}$ must be sufficiently small in order to describe the rheological behavior of a pseudoplastic fluid, but without creating numerical difficulties, due to too abrupt changes in the apparent viscosity near the point where $D_{II} = 0$. The analysis showed that for $D_{II} \leqslant 10^{-2}\ \mathrm{s}^{-1}$, the results are quite insensitive to the cut-off value. In the present work, a value of $D_{II} = 10^{-5}\ \mathrm{s}^{-1}$ is used.

3.7. Boundary conditions

The flow is assumed to be symmetrical with respect to the vertical plane containing the duct axis. In dimensionless coordinates system, the computational domain is $(r, \phi, X) \in [r_1, 1] \times [0, \pi] \times [0, X_f]$, where X_f is the final section.

The boundary conditions for V, W, U and Θ are:

$$r = r_1; \quad V = W = U = 0; \qquad \frac{\partial \Theta}{\partial r} = -1/(1 - r_1), \tag{10a}$$

$$r = 1; \quad V = W = U = 0; \qquad \frac{\partial \Theta}{\partial r} = 1/(1 - r_1), \tag{10b}$$

$$X = 0; \quad U = U_{fd}(r); \qquad V = W = 0; \qquad \Theta = 0, \tag{10c}$$

$$\phi = 0; \pi; \quad \frac{\partial U}{\partial \phi} = \frac{\partial V}{\partial \phi} = W = 0; \qquad \frac{\partial \Theta}{\partial \phi} = 0. \tag{10d}$$

The reference pressure at the inlet is set equal to zero. Using the dimensionless temperature Θ, K can be written as: $K = K_e \exp(-Pn\Theta)$, where K_e is the consistency at the inlet temperature, and Pn is the Pearson number: $Pn = (b\Phi R_2)/\lambda$. The expression of the fully developed axial velocity, $U_{fd}(r)$, is given by Bird et al. [11]. The problem is then governed by five dimensionless numbers: Gr, Pr, r_1, Pn and n.

The Nusselt numbers at the walls are defined by:

$$Nu_{1,2} = \frac{2(1-r_1)}{\Theta_{1,2} - \Theta_m},$$

where Θ_m is the bulk temperature and the subscripts $1, 2$ means inner or outer cylinder.

The mean values are based on the mean wall temperature averaged circumferentially:

$$\overline{Nu} = 2(1-r_1)/\left[\overline{\Theta}_{1,2} - \Theta_m\right], \quad \text{where } \overline{\Theta}_{1,2} = (1/\pi)\int_0^\pi \Theta_{1,2}\,\mathrm{d}\phi.$$

4. Numerical solution

Equations (4) and (6) constitute a parabolic system and can be solved by a stepwise integration in the axial direction from a specified set of upstream initial conditions. The conservation equations with the associated boundary conditions are discretized using a finite difference technique. The partial derivatives in the radial and azimuthal directions are approximated by a centered scheme, the first order derivatives in the axial direction are approximated by an upwind scheme. Special care was taken in calculating the terms containing $\partial\bar{\mu}_a/\partial r$. First, $\partial\bar{\mu}_a/\partial r$ is approximated by $(\bar{\mu}_{ai+1/2,j} - \bar{\mu}_{a_{i-1/2,j}})/Dr$. Near the region where $\partial U/\partial r \to 0$, a large viscosity gradient is present. Numerical instabilities may occur if $\bar{\mu}_{ai+1/2,j}$ or $\bar{\mu}_{ai-1/2,j}$ are calculated using linear interpolation. Patankar [12] describes a formulation for non-uniform viscosity that is based, for a uniform grid, on the harmonic mean rather than the arithmetic mean. In this work, we tested both linear and harmonic interpolations, reaching the conclusion that the harmonic interpolation produces more stable results. Similar methodology has been used by Ogawa et al. [13]. The procedure for the solution to the momentum and energy equations is based on the one proposed by Briley [14]. It starts by solving the finite difference form of the axial momentum equation for the U-field, assuming $\mathrm{d}P_m/\mathrm{d}X$. Based on this U-field, the overall continuity requirement of specified mass flow rate is checked. The residual mass defined in equation (11) coupled with a secant method, is used iteratively in correcting the U-field and P_m. The secant method converges in the limit of machine accuracy in three iterations.

$$\int_0^\pi \int_{r_1}^1 rU\,\mathrm{d}r\,\mathrm{d}\phi - \frac{\pi}{2}\left[1 - r_1^2\right] = Res. \tag{11}$$

When the residual flow rate, Res, calculated using Simpson rule, is less than or equal to 10^{-7}, the constraint (11) is assumed verified. The next step is the computation of the cross stream velocities from radial and tangential momentum equations using a pressure field $P'(r,\phi)$ of the upstream section. The results V_p and W_p (provisional velocity) are then corrected in order to satisfy the continuity equation:

$$V = V_p + V^*; \qquad W = W_p + W^*. \tag{12}$$

It is assumed that the velocity corrections are irrotational, and a velocity potential χ is introduced such that:

$$V^* = \frac{\partial \chi}{\partial r}; \qquad W^* = \frac{1}{r}\frac{\partial \chi}{\partial \phi}. \tag{13}$$

Substituting equations (12) and (13) into the continuity equation, a Poisson equation is readily found as:

$$\Delta \chi = f, \tag{14}$$

with homogeneous Neumann boundary conditions ($\partial \chi / \partial \mathbf{n} = 0$) on the computation domain boundaries. The pressure field $P'(r, \phi)$ is obtained by constructing a Poisson equation from radial and azimuthal momentum equations. All the boundary conditions are of Neumann type. Some care has to be taken in order to satisfy the divergence theorem (see Briley [14] and Fletcher [15]). After computing the flow variables, the energy equation is solved for the temperature field. The foregoing procedure has to be repeated until successive temperature fields do not change. These additional iterations could be avoided if the axial step is sufficiently small.

The momentum and energy equations are discretized using the two-step alternating direction, implicit method (A.D.I). The Poisson equations for the potential, χ, and the pressure, P, with the corresponding boundary conditions, are solved by line under successive relaxation with alternating sweeping direction. The criterion for convergence is $\max|\chi^{\ell+1} - \chi^{\ell}| / \max|\chi^{\ell+1}| \leqslant 10^{-5}$, ℓ is the iteration number, and $\max|P'^{\ell+1} - P'^{\ell}| / \max|P'^{\ell+1}| \leqslant 10^{-3}$. Finally, the overall algorithm is $\mathrm{O}(DX, (Dr)^2, (D\phi)^2)$.

Calculations were made for two radii ratios $r_1 = 0.5$ and 0.421. All the foregoing results were generated from a regular grid 101×101 in(r, ϕ) directions. The axial step was constant and equal to $2.5 \cdot 10^{-4}/L$.

4.1. Validation of the code

Since there is no analytical solution corresponding to the mixed convection flow under consideration, the program can be validated by comparison with the analytical solution for pure forced convection ($Gr = 0$), constant consistency ($b = 0$), one cylinder heated and the other one adiabatic. It is recalled that, according to Worsoe-Schmidt [16], the evolution of the Nusselt number with X^+, in the thermal inlet region for a Newtonian fluid, can be written as:

$$Nu_{new} = 1.3(1 - r_1)^{2/3} {\varphi_{new}}^{1/3} \left(X^+\right)^{-1/3}, \tag{15}$$

where φ_{new} is the dimensionless wall velocity gradient at the outer cylinder for Newtonian fluid and X^+ is the Cameron number: $X^+ = (2x^*/D_h)/Pe = X/2$. The subscript new denotes Newtonian fluid and D_h is the hydraulic diameter. For a pseudoplastic fluid, Tanaka and Mitsuichi [17] took into account the non-Newtonian behavior by multiplying the Newtonian Nusselt number by $\Pi^{1/3}$, where Π is the ratio of the wall velocity gradient to that obtained for a Newtonian fluid at the same flow rate:

$$Nu = \Pi^{1/3} Nu_{new}, \quad \text{where} \quad \Pi = \frac{(\partial U/\partial r)_{r=1}}{(\partial U/\partial r)_{new,r=1}}. \tag{16}$$

The computed circumferentially averaged Nusselt number at the outer cylinder for a grid size ranging from 21×21 to 101×101 is compared to the analytical solution given by equation (16). The results show that with the successive refined grid, the solution tends asymptotically towards the correct solution. For the grid size 101×101 the difference between the two solutions is less than 2% for $X^+ > 5 \cdot 10^{-5}$. The code is also validated by comparison with numerical results obtained by Nonino and Giudice [5] for simultaneous developing mixed convection flow in an annulus. Comparisons were made for the conditions: $Pr = 7$, $Re = 1000$, $Gr = 10^5$, and $r_1 = 0.5$. The two results differ by less than 2% for a grid size of 101×101.

5. Asymptotic solution

An asymptotic solution is developed in the entrance region, for deriving analytical expression of secondary flow velocities, wall temperature and local Nusselt number evolutions. It is obtained by perturbing the asymptotic forced convection solution at large Péclet numbers with small or moderate Reynolds numbers. First of all, the governing equations are written in a different dimensionless form since, in the entrance region, it is natural to refer lengths to the radius of a cylinder, and velocities to the mean axial velocity U_d: $u = u^*/U_d$, $v = v^*/U_d$, $w = w^*/U_d$. The pressure is non-dimensionalized by ρU_d^2. The dimensionless temperature is defined in terms of the inlet temperature and the wall heat flux density Φ:

$$\theta = \frac{(T - T_e)\lambda Pe^{1/3}}{\Phi R_2}.$$

The energy equation in dimensionless form becomes:

$$(\mathbf{v}.\nabla)\theta = \frac{1}{Pe}\nabla^2\theta.$$

For $Pe \to \infty$, temperature variations are confined to a small region (thermal boundary layer) adjacent to the wall. Thus, it is possible to resort to an asymptotic solution. Two zones, are then distinguished: the internal zone (thermal boundary layer) and the external zone (core region). In order to satisfy the least degeneracy principle [18], it can be shown that a gauge thickness δ of the internal zone [19] is: $\delta = Pe^{-1/3}$. Now, in performing the appropriate stretching of the coordinates within the internal zone, one have to require that in the overlap region between the internal and the external zones, the velocity components and all of their derivatives should stay continuous [20].

In the following analysis, the calculations are performed for the outer cylinder. A similar analysis can be obtained for the inner cylinder. We assume that for the first order, the Péclet number is sufficiently high ($Pe \gg 1$) so that there is no interaction between the inner and the outer thermal boundary layers.

5.1. Zero-order core flow

In the external zone, the core flow solution is obtained by expanding the depending variables into series in δ. It can be shown that the zero order solution is given by:

$$\theta_0^{ext} = 0; \qquad v_0^{ext} = 0; \qquad \frac{\partial P_0^{ext}}{\partial r} = w_0^{ext} = 0, \tag{17a}$$

$$u_0^{ext} = U_{fd}(r); \qquad \frac{\partial P_0^{ext}}{\partial x} = \left(\frac{\mathrm{d}P}{\mathrm{d}x}\right)_{fd}. \tag{17b}$$

It represents the undisturbed inlet conditions.

5.2. Zero-order boundary layer flow

The reader will note that in this paragraph, we do not use the superscript int for the internal variables.

In the internal zone, near the cylinder wall, the heat conduction normal to the wall becomes important. The radial coordinate r is stretched to reflect this physical fact. Accordingly, we introduce the inner variables, as in the classical boundary layer: $r = 1 - \delta\bar{r}$, $u = \delta\widehat{u}$, $v = -\delta^2\widehat{v}$ and $w = \delta\widehat{w}(\bar{r}, \phi, x)$. The temperature dependent consistency is expressed using a Taylor series expansion at the reference temperature T_e:

$$K = K_e\left[1 - \varepsilon_2\theta + \frac{\varepsilon_2^2}{2}\theta^2 + \mathrm{O}(\varepsilon_2^3)\right] = K_e\widetilde{K}, \quad \text{where } \varepsilon_2 = \frac{b\Phi R_2}{\lambda Pe^{1/3}} = \frac{Pn}{Pe^{1/3}}.$$

The solution can be expanded in a power series in terms of δ. Finally, after neglecting the smaller order terms, the governing equations can be written as:

$$\frac{\partial\widehat{v}}{\partial\bar{r}} + \frac{\partial\widehat{w}}{\partial\phi} + \frac{\partial\widehat{u}}{\partial x} = 0; \tag{18a}$$

$$\frac{1}{Pr}\left[\widehat{v}\frac{\partial\widehat{u}}{\partial\bar{r}} + \widehat{w}\frac{\partial\widehat{u}}{\partial\phi} + \widehat{u}\frac{\partial\widehat{u}}{\partial x}\right] = \frac{\partial}{\partial\bar{r}}\left[\widetilde{K}\left|\frac{\partial\widehat{u'}}{\partial\bar{r}}\right|^{n-1}\frac{\partial\widehat{u}}{\partial\bar{r}}\right]; \tag{18b}$$

$$\frac{1}{Pr}\left[\widehat{v}\frac{\partial\widehat{w}}{\partial\bar{r}} + \widehat{w}\frac{\partial\widehat{w}}{\partial\phi} + \widehat{u}\frac{\partial\widehat{w}}{\partial x}\right] = \varepsilon_1\theta\sin\phi + \frac{\partial}{\partial\bar{r}}\left[\widetilde{K}\left|\frac{\partial\widehat{u'}}{\partial\bar{r}}\right|^{n-1}\frac{\partial\widehat{w}}{\partial\bar{r}}\right]; \tag{18c}$$

$$\widehat{v}\frac{\partial\theta}{\partial\bar{r}} + \widehat{w}\frac{\partial\theta}{\partial\phi} + \widehat{u}\frac{\partial\theta}{\partial x} = \frac{\partial^2\theta}{\partial\bar{r}^2}, \tag{18d}$$

where, $\widehat{u'} = \widehat{u}/(\Pi\varphi_{newt})$ and $\varepsilon_1 = Gr/(RePe^{2/3})$. Two perturbation parameters ε_1 and ε_2 appear in the equations. A dependent variable 'A' can be expanded as double series in ε_1 and ε_2 as:

$$A = A_{00} + \varepsilon_1 A_{10} + \varepsilon_2 A_{01} + \varepsilon_1\varepsilon_2 A_{11} + \varepsilon_1^2 A_{20} + \varepsilon_2^2 A_{02} + \cdots,$$

where $A = \widehat{u}, \widehat{v}, \widehat{w}, \theta$. In the following, it is assumed that there is a parameter $\xi > 0$ such that $\varepsilon_1 = (\varepsilon_2)^{\xi}$. Three cases can be considered: $\xi > 1$, $\xi < 1$ and $\xi = 1$, depending on whether the effect of $K(T)$ is more important, less important or the same order to that of $\rho(T)$. Here, we consider the situation where, $\xi > 1$ ($\varepsilon_1 < \varepsilon_2$). However for $\xi \geqslant 2$, the product $\varepsilon_1\varepsilon_2 \leqslant \varepsilon_2^3$ and $\varepsilon_1 \leqslant \varepsilon_2^2$. In this article, the study is restricted to the case $1 < \xi < 2$. Homogeneous solutions are after that determined leading to the following expressions:

$$\widehat{u} = (ax)^{1/3}\eta\Pi\varphi_{new} + \varepsilon_1(ax)^2 H'_{10}\cos\phi + \varepsilon_2(ax)^{2/3}H'_{01} + \varepsilon_2^2(ax)H'_{02} + \varepsilon_1\varepsilon_2(ax)^{7/3}H'_{11}\cos\phi + \cdots, \tag{19a}$$

$$\widehat{v} = \varepsilon_1(ax)^{4/3}\Psi_{10}\cos\phi + \varepsilon_2\Psi_{01} + \varepsilon_2^2(ax)^{2/3}\Psi_{02} + \varepsilon_1\varepsilon_2(ax)^{5/3}\Psi_{11}\cos\phi + \cdots, \tag{19b}$$

$$\widehat{w} = \varepsilon_1(ax)F'_{10}\sin\phi + \varepsilon_1\varepsilon_2(ax)^{4/3}F'_{11}\sin\phi + \cdots, \tag{19c}$$

$$\theta = (ax)^{1/3}G_{00} + \varepsilon_1(ax)^2 G_{10}\cos\phi + \varepsilon_2(ax)^{2/3}G_{01} + \varepsilon_2^2(ax)G_{02} + \varepsilon_1\varepsilon_2(ax)^{7/3}G_{11}\cos\phi + \cdots. \tag{19d}$$

The functions H_{ij}, Ψ_{ij}, F_{ij}, and G_{ij} depend on η only, where, $\eta = \bar{r}/(ax)^{1/3}$ $(i, j = 0, 1)$ and $a = 9/(\Pi\,\varphi_{new})$. Substitution of the above expressions into the set of equations (18a)–(18d), and collecting terms of zero order which correspond to the situation of forced convection with $K = \text{const.}$, yields:

$$G''_{00} + 3\eta^2 G'_{00} - 3\eta G_{00} = 0.$$

The associated boundary conditions are:

$$G'_{00} = -1 \quad \text{at } \eta = 0;$$
$$G_{00} \to 0 \quad \text{as } \eta \to \infty.$$

The solution is:

$$G_{00}(\eta) = \frac{2}{3\,\Gamma(5/3)}\mathrm{e}^{-\eta^3} - \eta\left[1 - \frac{2}{\Gamma(5/3)}\int_0^{\eta}\xi\,\mathrm{e}^{-\xi^3}\mathrm{d}\xi\right].$$

It is the 'Lévêque' solution. It is interesting to note that $G_{00}(\eta)$ is independent of the flow behavior index n. One note that $G_{00}(0) = 0.738488$.

From the terms of order ε_1 which correspond to the perturbation of forced convection solution by the buoyancy force with $K = \text{const.}$, we obtain:

$$F_{10}''' + \frac{3}{Pr}\left[\eta^2 F''_{10} - 3\eta F'_{10}\right] = -G_{00};$$

$$n H_{10}''' + \frac{3}{Pr}\left[\eta^2 H''_{10} - 7\eta H'_{10} + 7H_{10}\right] = -\frac{9}{aPr} F_{10};$$

$$G''_{10} + 3\eta^2 G'_{10} - 18\eta G_{10} = \left[\Psi_{10} G'_{00} + \frac{a}{3} H'_{10}(G_{00} - \eta G'_{00})\right];$$

$$\Psi_{10}(\eta) = \frac{a}{3}\eta H'_{10}(\eta) - \frac{7a}{3} H_{10}(\eta) - F_{10}.$$

From the terms of order ε_2 which correspond to the perturbation of forced convection solution by the thermodependency of K with $\rho = \text{const.}$, we obtain:

$$n H_{01}''' + \frac{3}{Pr}\left[\eta^2 H''_{01} - 3\eta H'_{01} + 3H_{01}\right] = \frac{9}{a} G'_{00};$$

$$G''_{01} + 3\eta^2 G'_{01} - 6\eta G_{01} = \frac{a}{3}\left[H'_{01} G_{00} - 3H_{01} G'_{00}\right];$$

$$\Psi_{01} = \frac{a}{3}(\eta H'_{01} - 3H_{01}).$$

From the terms of order ε_2^2 which correspond to the perturbation of second order of forced convection solution by the thermodependency of K with $\rho = \text{const.}$, we obtain:

$$n H_{02}''' + \frac{3}{Pr}\left[\eta^2 H''_{02} - 4\eta H'_{02} + 4H_{02}\right]$$
$$= -\frac{9}{a}\left[G_{00} G'_{00} + G'_{01}\right] + \frac{2a}{9}(1-n) H''_{01} H'''_{01} + n\left[G'_{00} H''_{01} + G_{00} H'''_{01}\right] + \frac{a}{3Pr}\left[2H'^2_{01} - 3H_{01} H''_{01}\right];$$

$$G''_{02} + 3\eta^2 G'_{02} - 9\,\eta\, G_{02} = \frac{a}{3}\left[H'_{02} G_{00} - 4H_{02} G'_{00}\right];$$

$$\Psi_{02} = \frac{a}{3}(\eta H'_{02} - 4H_{02}).$$

From the terms of order $\varepsilon_1\varepsilon_2$ which correspond to the case of mixed convection with thermodependent consistency, we have:

$$n H_{11}''' + \frac{3}{Pr}\left[\eta^2 H''_{11} - 8\eta H'_{11} + 8H_{11}\right]$$
$$= \frac{9}{a} G'_{10} + n\frac{\mathrm{d}}{\mathrm{d}\eta}(G_{00} H''_{10}) + \frac{1}{Pr}\left[\Psi_{10} H''_{01} - \frac{a\eta}{3} H'_{10} H''_{01} + \Psi_{01} H''_{10} - \frac{a\eta}{3} H'_{01} H''_{10}\right] + \frac{1}{Pr}\left[\frac{8a}{3} H'_{01} H'_{10} - \frac{9}{a} F_{11}\right];$$

$$F_{11}''' + \frac{3}{Pr}\left[\eta^2 F''_{11} - 4\eta F'_{11}\right]$$
$$= -G_{01} + \frac{a}{Pr}\left[H'_{01} F'_{10} - H_{01} F''_{10}\right] - \frac{(n-1)\,a}{9}\frac{\mathrm{d}}{\mathrm{d}\eta}(F''_{10} H''_{01}) + \frac{\mathrm{d}}{\mathrm{d}\eta}(G_{00} F''_{10});$$

$$G''_{11} + 3\eta^2 G'_{11} - 21\eta G_{11}$$
$$= \left[\Psi_{10} G'_{01} + \Psi_{01} G'_{10} + \Psi_{11} G'_{00}\right] + \frac{a}{3}\left[H'_{01}(6G_{10} - \eta G'_{10}) + H'_{10}(2G_{01} - \eta G'_{01})\right] + \frac{a}{3} H'_{11}\left[G_{00} - \eta G'_{00}\right];$$

$$\Psi_{11} = -F_{11} + \frac{a}{3}(\eta H'_{11} - 8H_{11}),$$

with the associated boundary conditions:

$$\begin{cases} F_{10} = F'_{10} = H_{10} = H'_{10} = G'_{10} = 0 \quad \text{at } \eta = 0, \\ F'_{10} = G_{10} = H''_{10} \to 0 \quad \text{as } \eta \to \infty, \end{cases}$$

$$\begin{cases} H_{01} = H'_{01} = G'_{01} = 0 \quad \text{at } \eta = 0, \\ H''_{01} = G_{01} \to 0 \quad \text{as } \eta \to \infty, \end{cases}$$

$$\begin{cases} H_{02} = H'_{02} = G'_{02} = 0 \quad \text{at } \eta = 0, \\ H''_{02} = G_{02} \to 0 \quad \text{as } \eta \to \infty, \end{cases}$$

$$\begin{cases} F'_{11} = H'_{11} = G'_{11} = 0 \quad \text{at } \eta = 0, \\ F'_{11} = H''_{11} = G_{11} \to 0 \quad \text{as } \eta \to \infty, \end{cases}$$

The boundary layer velocities u and v along the outer edge of the boundary are obtained by taking the limit of equations (19a)–(19b) as $\eta \to \infty$.

The set of ordinary differential equations are integrated numerically using a fourth-order Runge–Kutta method with shooting. The values of $H''_{10}(0)$, $F''_{10}(0)$, $H''_{01}(0)$, $G_{01}(0)$, $G_{10}(0)$ are given in appendix.

Remark: The expansion (19a)–(19d) breaks down at a distance of X_c^+, where the buoyancy cross flow effects become as important as the forced convection effects. According to Bejan [21] the type of convection mechanism is decided by the smaller of the two scales of thermal boundary layer: $\delta_{t,fc}$ (pure forced convection) and $\delta_{t,nc}$ (pure natural convection).

– For pure forced convection, fully developed flow and large Prandtl number, the scaling analysis applied to the energy equation leads to:

$$\delta_{t,fc}/R_2 \sim \left((1-r_1)X^+/\Pi\varphi_{new}\Pi^*\right)^{1/3},$$

where Π^* is the modification of the wall axial velocity gradient by the thermodependency of K [22]. The expression of Π^* as a function of the working parameters is given in section 6. For a large Prandtl number, the local velocity field adjusts almost instantaneously to the local temperature, so that temperature variations are small everywhere, except in the very thin layer $\delta_{t,fc}$. As a result, viscosity variations are not sufficiently large to cause significant variation in the pressure drop (Ockendon et al. [23], Richardson [24]). It then follows that the dependence of τ_{rx} upon the axial position can be neglected. Therefore, $\mu_a = \mu_0/\Pi^*$.

– For pure natural convection, the scaling analysis follows those performed for the boundary layer along infinite vertical plates [21,25]. When the Prandtl number is large, the scaling analysis applied to the conservation equations yields the classical result:

$$\delta_{t,nc}/R_2 \sim \left[1/(\Pi^* \times Ra)\right]^{1/5},$$

where Ra is the Rayleigh number, $Ra = GrPr$. The same apparent viscosity is used for both convection mechanisms.

A new parameter Γ is defined, $\Gamma = \delta_{t,fc}/\delta_{t,nc}$. For the outer cylinder, Γ is given by:

$$\Gamma = \frac{\delta_{t,fc}}{\delta_{t,nc}} \sim \left(\frac{(1-r_1)^{1/3}X^{+1/3}Ra^{1/5}}{(\Pi\varphi_{new})^{1/3}\Pi^{*2/15}}\right). \tag{20}$$

Similar results are obtained for the inner cylinder. The transition from forced convection to natural convection occurs approximately at $\Gamma = 1$. We define X_c^+ the critical Cameron number for which this condition is satisfied. When $\Gamma < 1$ (i.e. $X^+ < X_c^+$), forced convection dominates and when $\Gamma > 1$ (i.e. $X^+ > X_c^+$), natural convection dominates.

6. Analysis of results and discussion

In order to distinguish between the effect of variable consistency $K(T)$, non-Newtonian behavior and free convection on the flow dynamics and on heat transfer, the results are presented in three separated parts. The first one corresponds to the case of forced convection with $K(T)$. The second one (section 6.2) deals with the mixed convection problem with constant consistency. The case of mixed convection with variable consistency is presented in section 6.3.

Remark: The asymptotic solutions for the outer and inner cylinders are similar. In order to avoid redundancy, the results obtained from asymptotic analysis are given only for the outer cylinder.

6.1. Forced convection with variable consistency

In the case of forced convection coupled with a consistency variation with temperature, the flow structure is characterized by a displacement of fluid particles from the core region towards the heated wall. At first order, this displacement is represented in an asymptotic solution by the second term $\varepsilon_2\Psi_{01}$ of equation (19b). The wall velocity gradient increases and the axial velocity in the central zone of the annular gap decreases to maintain flow rate conservation. *Figure 2* illustrates axial velocity profiles obtained at four axial positions. The deformation rate of the axial velocity profile decreases along the heating zone. As a matter of fact, in the boundary layer, the flow is quickly accelerated from the entrance, then the acceleration declines downstream. This is in agreement with the asymptotic solution given by:

$$\frac{\partial \widehat{u}}{\partial x} = \varepsilon_2 \frac{a}{3\,(ax)^{1/3}}\left[2H'_{01} - \eta H''_{01}\right] + \mathrm{O}\left(\varepsilon_2^2\right).$$

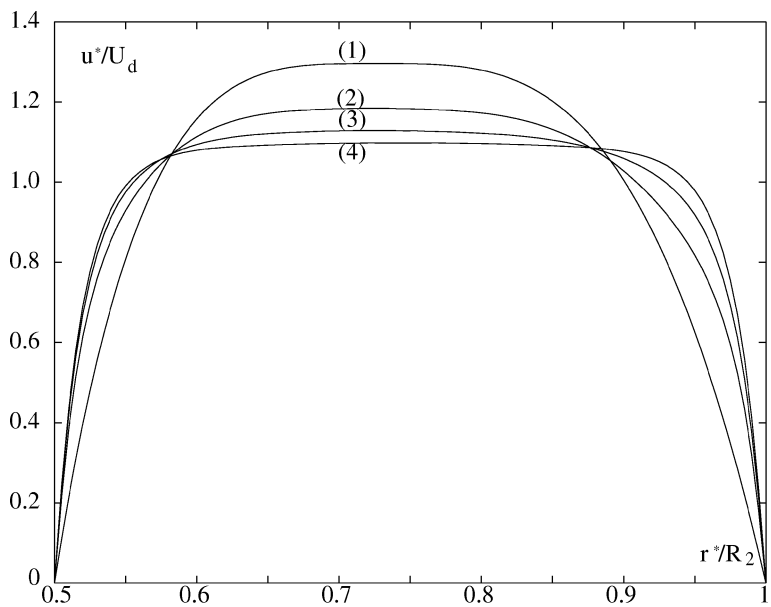

Figure 2. Evolution of the axial velocity profile along the heating zone for $Gr = 0$, $Re = 40$, $Pr = 348.3$, $Pn = 16$, $n = 0.4$ and $r_1 = 0.5$: (1) $X^+ = 0$; (2) $X^+ = 0.9 \cdot 10^{-3}$; (3) $X^+ = 3.6 \cdot 10^{-3}$; (4) $X^+ = 1.8 \cdot 10^{-2}$.

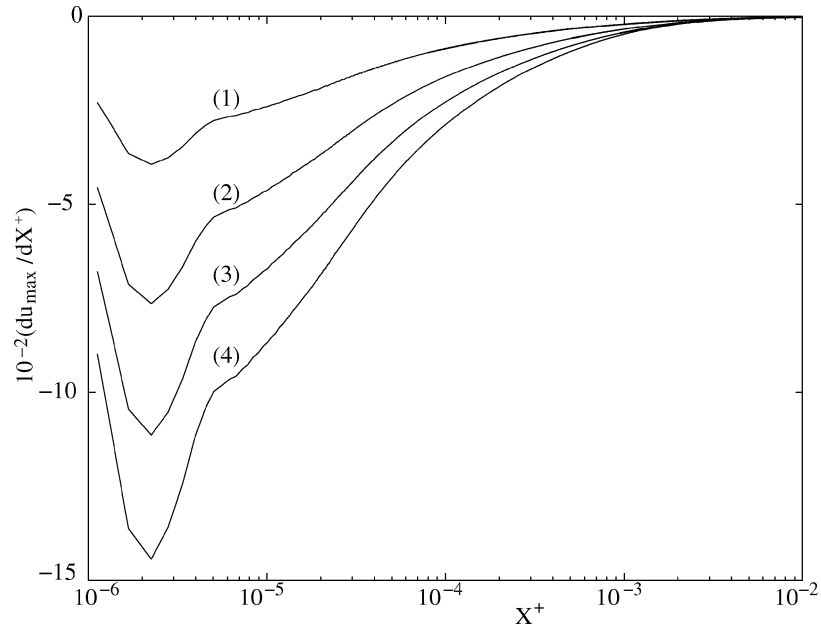

Figure 3. Evolution of the axial acceleration along the heating zone for $Gr = 0$, $Re = 40.0$, $Pr = 348.3$, $n = 0.4$ and $r_1 = 0.5$: (1) $Pn = 5.32$; (2) $Pn = 10.66$; (3) $Pn = 16$; (4) $Pn = 21.33$.

Conversely, the flow in the central zone of the annular gap is rapidly decelerated from the entrance section, then the deceleration diminishes as $\varepsilon_2(ax)^{-1/3}$. *Figure 3* shows the evolution of $\partial U_{\max}/\partial X^+$ as a function of X^+, for $r_1 = 0.5, n = 0.4$ and for different values of Pn. Here, $U_{\max}$ is the maximum axial velocity.

The modification of the wall axial velocity gradient due to $K(T)$, can be characterized by the ratio Π^*. From the asymptotic solution, we have:

$$\Pi^* = \frac{|\partial u/\partial r|_{r=1,x}}{|\partial u/\partial r|_{r=1,x=0}} = 1 + \varepsilon_2 \frac{(ax)^{1/3} H''_{01}(0)}{\Pi\,\varphi_{new}} + \mathrm{O}(\varepsilon_2^2).$$

For a large Prandtl number:

$$\Pi^* \approx 1 + \varepsilon_2 (ax)^{1/3} \frac{G_{00}(0)}{n} = 1 + \frac{b\Phi R_2}{\lambda\, n} \left(\frac{9x}{\Pi \varphi_{new} Pe} \right)^{1/3} G_{00}(0).$$

This latter expression for Π^* can also be obtained from the original conservation equation, using the assumptions of Ockendon and Ockendon [23] and Richardson [24], where for large Pr and $X^+ \ll 1$, the dependence of τ^*_{rx} upon X^+ can be neglected.

$$\Pi^* \approx \left[\frac{K_{r=1,x=0}}{K_{r=1,x}} \right]^{1/n} = \exp\bigl[b(T_p - T_e)/n\bigr] \approx 1 + \frac{b(T_p - T_e)}{n}.$$

The temperature difference $(T_p - T_e)$ is calculated at a first approximation, using the Lévêque solution: $(ax/Pe)^{1/3}(\Phi R_2/\lambda)G_{00}(0)$.

Π^* increases along the heating zone. This increase is more important at the outer cylinder where the wall temperature is higher than that of the inner one. This is due to the asymmetry of the axial velocity profile at the entrance section where $|\partial u/\partial r|_{2,x=0} < |\partial u/\partial r|_{1,x=0}$. For power law fluids, the analysis of the function $\Pi^*(n)$, for n ranging between 0.3 and 1, shows that Π^* increases when n decreases. Hence, the thermodependency

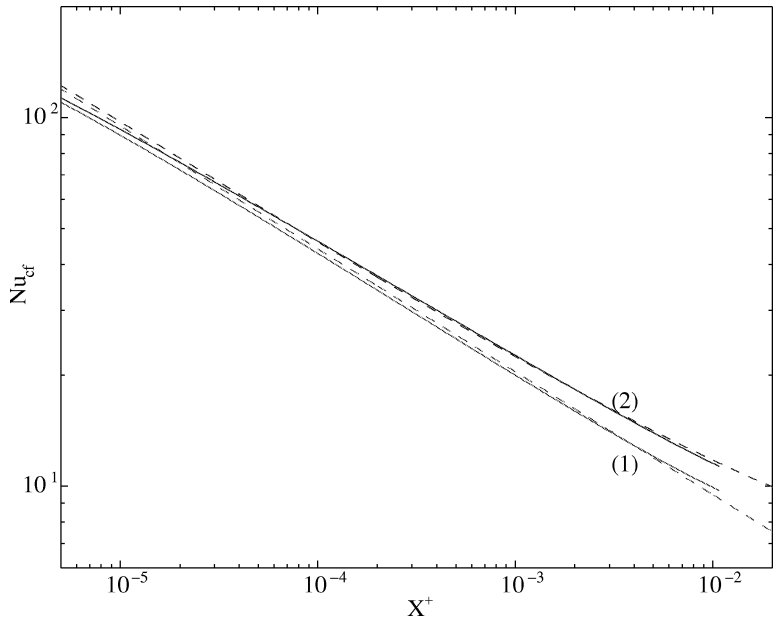

Figure 4. Evolution of the external Nusselt number along the heating zone for $Gr = 0$, $n = 0.4$ and $r_1 = 0.5$: (1)$Pn = 0$; (2)$Pn = 8$; (- - -) asymptotic solution; (—) numerical solution.

effect of K is more characterized with increased the shear thinning of the fluid. This result conforms to the corrective factor for Nusselt correlations proposed by Mizushina et al. [26] and Joschi and Bergles [27].

The local axial shear stress is computed from:

$$\tau^*_{rx} = K\left(\frac{U_d}{R_2}\right)^n \left(-\frac{\partial u}{\partial r}\right)^{n-1} \left(\frac{\partial u}{\partial r}\right).$$

Using the series expansion (19a)–(19d), the effect of thermodependency on the axial shear stress can be illustrated by the ratio:

$$\frac{\tau^*_{rx,th}}{\tau^*_{rx,nth}} = 1 - \varepsilon_2 (ax)^{1/3} G_{00}(0) + \frac{n\varepsilon_2}{(\Pi\varphi_{new})}(ax)^{1/3} H''_{01}(0) + \mathrm{O}(\varepsilon_2^2). \tag{21}$$

The second and the third terms are opposing. In fact, the second term reduces the shear stress due to the decrease of K with T and the third term increases the shear stress due to the increase of the axial velocity gradient.

According to the temperature distribution, the isotherms are concentric and the heat transfer coefficient at the heated wall, increases with the Pearson number as expected. The evolution of the external Nusselt number along the heating zone is depicted in *figure 4*, for $n = 0.4, Pn = 0$ and $Pn = 8$. The asymptotic solutions are exemplified by dashed lines. The local Nusselt number can be written as:

$$\frac{Nu_{th}}{Nu_{nth}} = \frac{G_{00}(0)}{G_{00}(0) + \varepsilon_2 (ax)^{1/3} G_{01}(0) + \mathrm{O}(\varepsilon_2^2)}, \tag{22}$$

with $Nu_{nth} = 2(1 - r_1)Pe^{1/3}/[(ax)^{1/3} G_{00}(0)]$. The numerical calculations performed for a radius ratio of 0.5 and n ranging between 0.3 and 1, indicate that the modification of Nusselt number (Nu_{th}/Nu_{nth}) by the thermodependency $K(T)$ increases with increasing the shear thinning of the fluid. A similar evolution is obtained for the internal Nusselt number.

6.2. Mixed convection with constant consistency

The case of mixed convection, where K remains constant, is now considered. According to the density variation, the warmer fluid moves upward ($w > 0$) along the heated walls of the cylinders and the colder one moves downward ($w < 0$) in the core region (see *figure 5*). Along the vertical line, where $w = 0$, there are

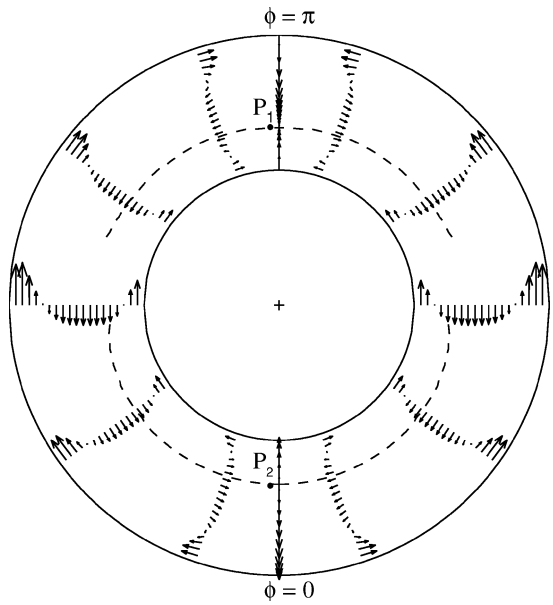

Figure 5. Secondary flow structure at $X^+ = 3.6 \cdot 10^{-3}$ for $Re = 40$, $n = 0.7$, $r_1 = 0.5$, $Gr = 20480$, $Pn = 0$ and $Pr = 348.3$.

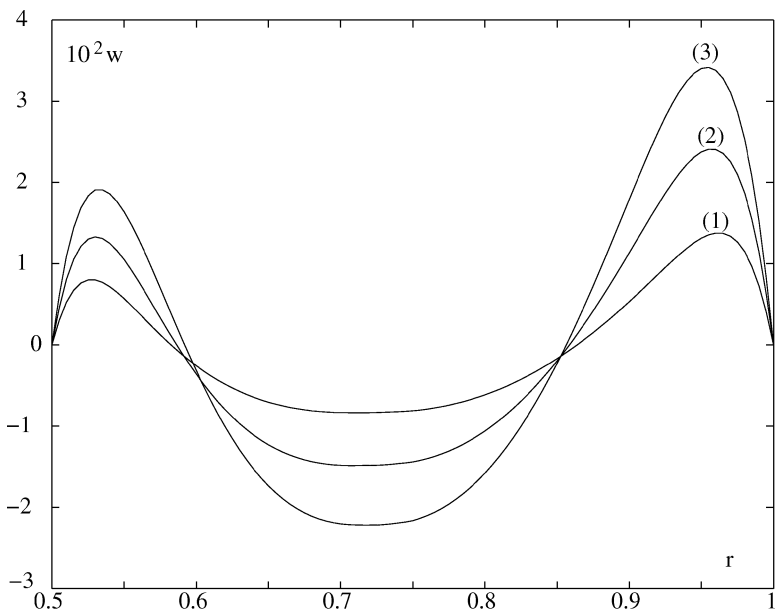

Figure 6. Azimuthal velocity profiles for $\phi = \pi/2$, $n = 0.4$, $r_1 = 0.5$, $Gr = 20480$, $Pr = 348.3$ and $Re = 40$: (1) $X^+ = 8.97 \cdot 10^{-4}$; (2) $X^+ = 1.8 \cdot 10^{-3}$; (3) $X^+ = 3.6 \cdot 10^{-3}$.

Table II. Effect of the flow behavior index on the thermal stratification for $r_1 = 0.5$, $Re = 40$, $Pr = 348{,}3$ and $Gr = 20480$.

n		$X^+ = 8.97 \cdot 10^{-4}$	$X^+ = 1.8 \cdot 10^{-3}$	$X^+ = 3.60 \cdot 10^{-3}$
1	S_1	0.056	0.162	0.510
	S_2	0.046	0.153	0.483
0.4	S_1	0.028	0.077	0.207
	S_2	0.023	0.076	0.240

two saddle points, (P_1) and (P_2) which move slightly along the heating zone, towards the inner cylinder. The dashed line corrresponds to the positions where $V = 0$. The flow structure in the section of the annular gap can be viewed as two counter-rotating cells. The analysis of the tangential velocity profiles at a given axial position and for different azimuthal positions shows that the fluid is accelerated between the lower part of the annular duct and roughly the median plane, it is then decelerated between the median plane and the upper part of the duct. Near the entrance section, w varies as $\sin(\phi)$, in agreement with the asymptotic solution: $\widehat{w} \approx \varepsilon_1 (ax) F'_{10} \sin(\phi)$.

Each tangential velocity profile exhibits two maxima, one near the outer cylinder $w_{\max,2}$ and the other one near the inner cylinder $w_{\max,1}$. For a large Prandtl number, the radial position of $w_{\max}$ at $\phi = \pi/2$ can be determined from the thickness δ_t of the thermal boundary layer [21,28]: $\delta_t / R_2 = (ax/Pe^{1/3}) G_{00}(0)$, and $\eta(w_{\max}) = G_{00}(0)$. The stratification S at the inner and outer cylinders are defined by: $S_{1,2} = [\Theta_{t1,2} - \Theta_{b1,2}]/[\Theta_{1,2m} - \Theta_m]$. The subscripts t and b denote top and bottom of the duct, respectively. The values of $S_{1,2}$ for $n = 1$ and 0.4 and at different axial positions are reported in *table II*. As expected, S increases along the heating zone and decreases with the shear thinning of the fluid. Near the entrance section, the evolution of S is quite well described by the asymptotic solution given by: $S \approx 2\varepsilon_1 (ax)^{5/3} |G_{10}(0)| / G_{00}(0)$. The corresponding azimuthal velocity profiles are shown in *figure 6*. One can note that $w_{\max,2} > w_{\max,1}$

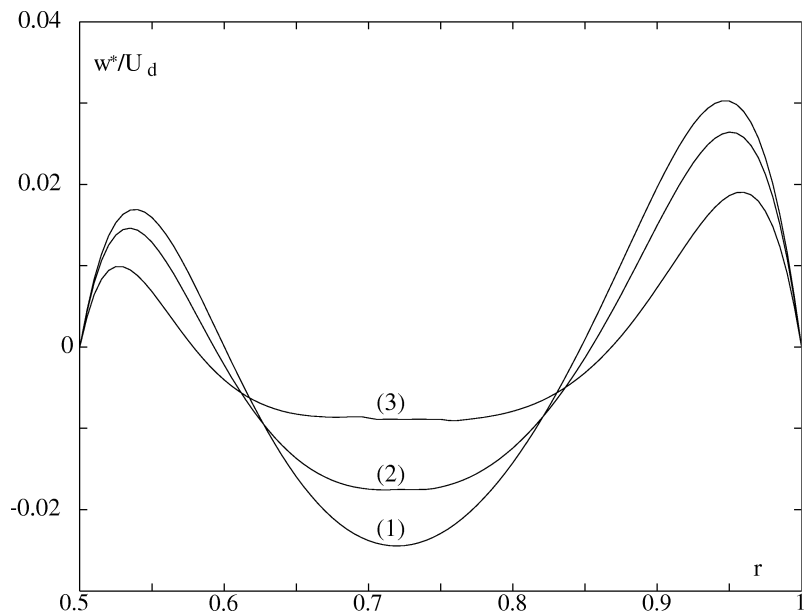

Figure 7. Effect of flow behavior index on the tangential velocity profile for $\phi = \pi/2$, $r_1 = 0.5$, $Re = 40$, $Pr = 348.3$, $Gr = 20480$ and $X^+ = 3.6 \cdot 10^{-3}$: (1) $n = 1$; (2) $n = 0.7$; (3) $n = 0.4$.

Table III. Effect of the flow behavior index on the maxima of azimuthal velocity for $r_1 = 0.5$, $Re = 40$, $Pr = 348{,}3$ and $Gr = 20480$.

n		$X^+ = 8.97 \cdot 10^{-4}$	$X^+ = 1.8 \cdot 10^{-3}$	$X^+ = 3.60 \cdot 10^{-3}$
0.7	$\frac{[w_{2,\max}]_{nnew}}{[w_{2,\max}]_{new}}\Pi_2$	0.95	0.95	0.98
	$\frac{[w_{1,\max}]_{nnew}}{[w_{1,\max}]_{new}}\Pi_1$	1.01	1.01	1.02
0.4	$\frac{[w_{2,\max}]_{nnew}}{[w_{2,\max}]_{new}}\Pi_2$	0.85	0.84	0.89
	$\frac{[w_{1,\max}]_{nnew}}{[w_{1,\max}]_{new}}\Pi_1$	0.99	0.97	0.93

because $|\partial U/\partial r|_{2,x=0} < |\partial U/\partial r|_{1,x=0}$. Concerning the flow behavior effect on secondary flow, *figure 7*, gives the azimuthal velocity profiles at $X^+ = 3.6 \cdot 10^{-3}$ for $\phi = \pi/2$ and $n = 0.4; 0.7$ and 1. It shows that the shear thinning of the fluid induces a decrease of w, and the maximum of w is shifted towards the heated walls. This evolution can be explained as follows: the shear thinning ($n < 1$) induces an increase of the wall axial velocity gradient (Π), consequently, a decrease of the thermal boundary layer thickness and by there, that associated to the secondary flow. It is clear from asymptotic solution that $w_{\max,nnew}/w_{\max,new} = \Pi^{-1}$ and $(1 - r_{\max,nnew})/(1 - r_{\max,new}) = \Pi^{1/3}$. Here, the subscript, $nnew$, denotes non-Newtonian. This result is in agreement with the numerical solution as it is shown in *table III*. The secondary flow intensity may be characterized by the maximum value of the cross stream velocity $I_{sf} = \sqrt{V^2 + W^2}$. The evolution of I_{sf} is illustrated in *figure 8*, for $n = 1$ and 0.4. The asymptotic solution, $w_{\max}$, is also represented in the graph by dashed lines. For the situations considered in this paper, v is one order less than w, therefore, $I_{sf} \approx w_{\max}$. From the entrance section, I_{sf} increases linearly as $\varepsilon_1(ax)$, reaches a maximum, and decreases slightly towards an asymptotic value that is corresponding to the fully developed dynamic regime.

As a consequence, of the upward motion near the heated walls, and downward one in the core region, results a radial motion of the fluid particles. They enter the boundary layer at the lower part of the duct and leave it at the upper part. This corresponds to $v \approx -\varepsilon_1(ax)^{4/3}\psi_{10}\cos(\phi)/Pe^{2/3}$ deduced from the asymptotic solution (equations (19b)). The axial flow is accelerated at the lower half of the annular duct as $\varepsilon_1(ax)/Pe^{1/3}$ and decelerates at the upper half with the same rate. The average acceleration equals zero.

The local wall shear stress is given by:

$$\tau^*_{rx} = K\left(\frac{U_d}{R_2}\right)^n\left(-\frac{\partial u}{\partial r}\right)^{n-1}\left(\frac{\partial u}{\partial r}\right) \quad \text{and} \quad \tau_{r\phi} = K\left(\frac{U_d}{R_2}\right)^n\left(-\frac{\partial u}{\partial r}\right)^{n-1}\left(\frac{\partial w}{\partial r}\right).$$

Using the series expansion, it is found that the effect of the secondary flow can be described by the following relations:

$$\frac{\tau^*_{rx}}{\tau^*_{rx,fc}} = 1 + n\varepsilon_1(ax)^{5/3}\frac{H''_{10}(0)\cos(\phi)}{\Pi\varphi_{new}} + \mathrm{O}(\varepsilon_1^2),$$

$$\tau^*_{r\phi} = \varepsilon_1\frac{\mu_0 U_d}{R_2}(ax)^{2/3}F''_{10}(0)\sin(\phi) + \mathrm{O}(\varepsilon_1^2).$$

At $\phi = \pi$, the secondary flow reduces the shear stress as $(ax)^{5/3}$ increases, with a possibility of separation.

The upward movement of the warmer fluid and downward movement of the colder fluid lead progressively to the appearance of a low density fluid layer along the heating zone, with a higher temperature at the upper

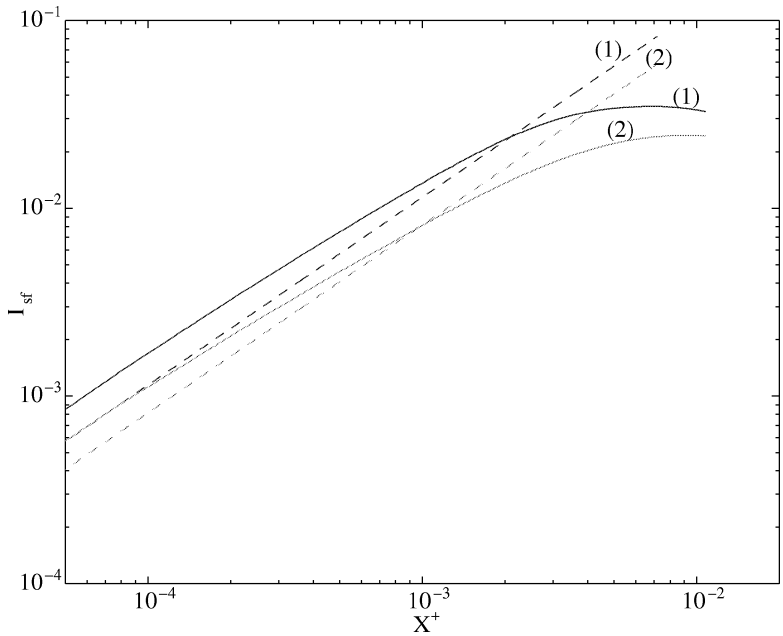

Figure 8. Variation of the maximum value of cross-stream velocity with axial position for $Gr = 20480$, $Re = 40$ and $Pr = 348.3$: (1) $n = 1$; (2) $n = 0.4$; (- - -) asymptotic solution; (—) numerical solution.

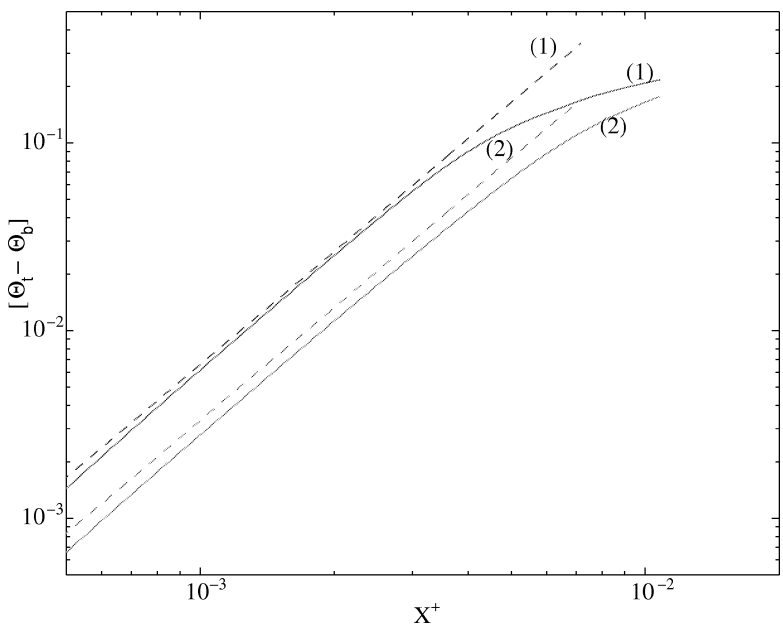

Figure 9. Dimensionless temperature difference between the top and the bottom of the outer cylinder along the heated region for $Re = 40$, $Gr = 20480$ and $Pr = 348.3$: (1) $n = 1$; (2) $n = 0.4$; (- - -) asymptotic solution; (—) numerical solution.

part of the annular duct. The colder fluid is confined in the lower part. *Figure 9*, gives $[\Theta]_b^t = [\Theta_t - \Theta_b]$ as a function of X^+, for $n = 0.4$ and 1. The asymptotic solution is plotted in the graph by dashed lines. In the entrance region ($X^+ < X_c^+$), using equation (19d), the increase of $[\Theta]_b^t$ as X^+ increases, can be described

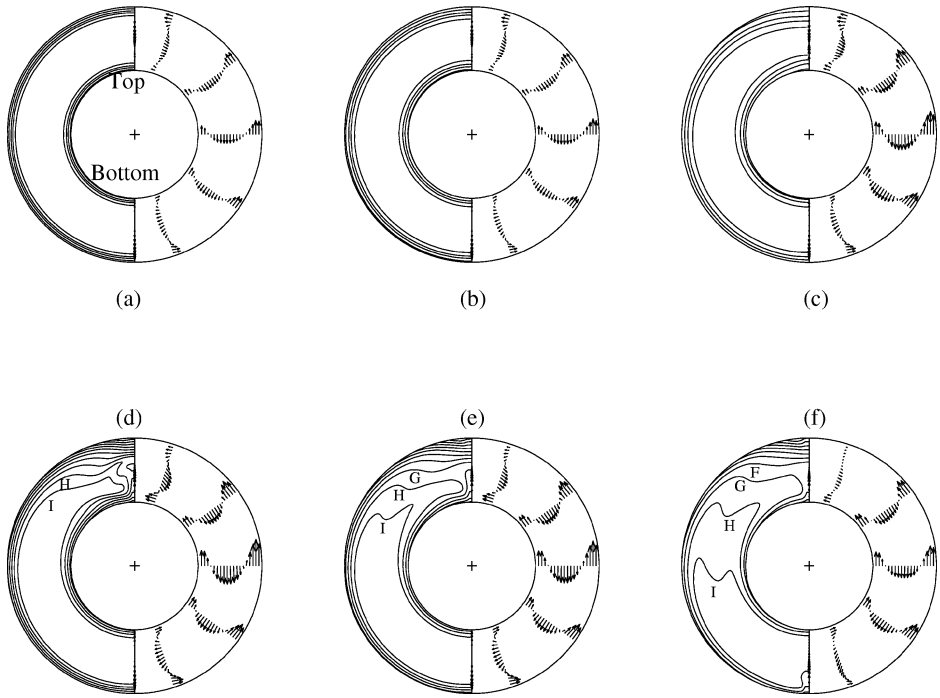

Figure 10. Isovalues of $(T - T_e)/(T_{\max} - T_e)$ at left, and secondary flow at right, for $Re = 40$, $Gr = 20480$, $Pr = 348.3$, $n = 0.7$ and $r_1 = 0.5$. Isovalues: $A = 0.9$, $B = 0.8$ then with a step of 0.1 until $I = 0.2$. In the following, the isotherms are given from the heated wall to the core flow: (a) $X^+ = 8.97 \cdot 10^{-4}$, four isotherms B, E, G, I; (b) $X^+ = 1.8 \cdot 10^{-3}$, four isotherms B, E, G, I; (c), $X^+ = 3.6 \cdot 10^{-3}$, four isotherms B, E, G, I; (d) $X^+ = 7.2 \cdot 10^{-3}$, isotherms A to I; (e) $X^+ = 1.2 \cdot 10^{-2}$, isotherms A to I; (f) $X^+ = 1.8 \cdot 10^{-2}$, isotherms A to I.

by: $[\Theta]_b^t \approx 8(1 - r_1)^4 GrPr(aX^+)^2 |G_{10}(0)|$. *Figure 9* shows also that $[\Theta]_b^t$ decreases with increasing the shear thinning of the fluid. This is due to the decrease of the recirculation intensity when n decreases as indicated previously.

The isotherms and the secondary flow for different axial positions are represented in *figure 10*. Near the entrance section, the isotherms are practically concentric circles since the forced convection is dominating in the heat transfer mechanism. As the fluid moves downstream, the secondary flow becomes stronger and the isotherms are gradually distorted. They are closely spaced at $\phi = 0$ and sparsely spaced at $\phi = \pi$. This indicates a deterioration of heat transfer coefficient in the upper part of the annular duct and an improvement in the lower part as predicted by the asymptotic solution:

$$\frac{Nu}{Nu_{fc}} \approx \frac{1}{1 + \varepsilon_1 (ax)^{5/3} [G_{10}(0)/G_{00}(0)] \cos(\phi)}. \tag{23}$$

Equations (19a) and (23) indicate that the secondary flow effect on the wall temperature and Nusselt number grows rapidly downstream and is proportional to $(ax)^{5/3}$. This means that an initially small secondary effect, becomes dominant flow component further downstream. One can write that when $\varepsilon_1 (ax)^{5/3}$ is O(1), the free convection effect becomes important. This assumption leads to the similar expression for X_c^+ determined from scaling analysis.

The variation along the heating zone of the external circumferentially averaged Nusselt number $\overline{Nu}$ for $n = 0.4$ and $n = 1$ is shown in *figure 11*. The broken lines correspond to forced convection ($Gr = 0$). Different regions can be distinguished according to the importance of the forced convection with respect to the natural convection. Near the entrance section (here$X^+ < X_c^+ \approx 10^{-3}$), $\overline{Nu}$ decreases with X^+. The free

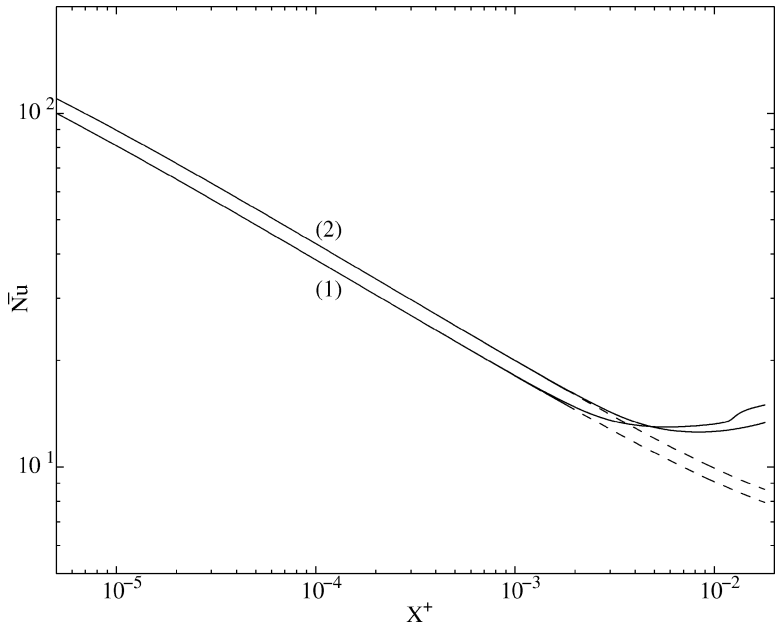

Figure 11. Evolution of the external circumferentially averaged Nusselt number along the heating zone for $r_1 = 0.5$; $Pr = 348.3$; $Gr = 20480$. Flow behavior index effect: (1) $n = 1$; (2) $n = 0.4$; $(- - -)$ forced convection.

Table IV. Comparison between X_c^+ from a scaling analysis and X_c^+ from the numerical solution for $r_1 = 0.5$, $Pr = 348.3$ and $Gr = 20480$.

n	1	0.7	0.4
$(X_c^+)_{sc,2}$	$1.69 \cdot 10^{-3}$	$1.88 \cdot 10^{-3}$	$2.38 \cdot 10^{-3}$
$\left[\frac{(X_c^+)_{num}}{(X_c^+)_{sc}}\right]_1$	0.80	0.80	0.83
$\left[\frac{(X_c^+)_{num}}{(X_c^+)_{sc}}\right]_2$	0.82	0.83	0.9

convection effects are weak, and all the curves fall on that corresponding to the forced convection. Beyond the point $X^+ = X_c^+$, the buoyancy becomes important and the curves for mixed convection rise above the forced convection one. A minimum of $\overline{Nu}$ is obtained at $X^+ = X_m^+$ due to the combined thermal entrance and buoyancy effects. From X_m^+ , natural convection is the dominant mechanism, $\overline{Nu}$ increases with X^+ and tends asymptotically to a fully developed value. According to Orfi et al. [29], the location X_m^+ corresponds roughly to the axial position where the secondary flow is the most vigorous (see *figure 8*). In the first region, $\overline{Nu}$ increases when n decreases, due to the increase of wall axial velocity gradient. However, in the second region, $X^+ > X_c^+$, $\overline{Nu}$ decreases with the shear thinning of the fluid, due to the decrease of the secondary flow intensity.

Concerning the critical axial position X_c^+, where the $\overline{Nu}$ curve for mixed convection begins to depart from its forced convection counterpart, we obtain from scaling analysis (see equation (20)): $X_c^+ = \mathrm{O}(\Pi\varphi_{newt}/[(1 - r_1)Ra^{3/5}])$. It is found that X_c^+ decreases with the Rayleigh number and with the shear thinning of the fluid. *Table IV* gives the ratio $X_{c,num}^+/X_{c,sc}^+$, where, the subscripts num and sc refer to the numerical and scale analysis respectively. Here, $X_{c,num}^+$ is defined such that $(Nu_{Gr\neq 0} - Nu_{Gr=0})/Nu_{Gr=0} = 1\%$. The values of $X_{c,num}^+/X_{c,sc}^+$ are ~ 1, validating then, the criterion used for the determination of X_c^+ from scaling analysis.

6.3. Mixed convection with variable consistency

The results corresponding to mixed convection with thermodependent consistency are now analyzed. The decrease of K as T increases, on one hand reduces the drag forces of viscous origin, thereby increasing the intensity of the secondary flow, and on the other hand increases the wall axial velocity gradient, which in turn decreases the thermal boundary layer thickness and therefore, that associated to the secondary flow. This is illustrated in *figure 12*, where tangential velocity profiles are presented at $X^+ = 1.01 \cdot 10^{-2}$, $\phi = \pi/2$, $n = 0.7$ and for three values of *Pn*: 0; 6 and 16. The maximum, $w_{\max}$, of the tangential velocity increases and its radial location, $r(w_{\max})$ is shifted towards the heated wall, with increasing *Pn*. Near the entrance section, and using equation (19c), we have:

$$w_{\max,th} - w_{\max,nth} \approx \frac{\varepsilon_1\varepsilon_2}{Pe^{1/3}}(ax)^{4/3} = \frac{GrPn}{Re}\left(\frac{ax}{Pe}\right)^{4/3}.$$

For a large Prandtl number and at a first order:

$$r(w_{\max,nth}) - r(w_{\max,th}) = \frac{\varepsilon_2}{Pe^{1/3}}(ax)^{2/3}G_{01}(0) = Pn\left(\frac{ax}{Pe}\right)^{2/3}G_{01}(0).$$

The increase of the secondary flow intensity with *Pn*, indicated above, induces an increase of the wall temperature difference, $[\theta]_b^t$ between the top and the bottom:

$$[\theta_{th}]_b^t - [\theta_{nth}]_b^t \approx 2\varepsilon_1\varepsilon_2(ax)^{7/3}\left|G_{11}(0)\right|.$$

The thermal field structure is illustrated in *figures 13, 14* and *15*. *Figure 13* shows the distortion of the isotherms along the heating zone. It is qualitatively similar to that obtained for $K = \text{const}$. However, near the inlet, the asymptotic solution provides higher stratification: $S_{th} > S_{nth}$. *Figure 14* gives the evolution of the outer cylinder wall temperature at $\phi = 0$ and $\phi = \pi$ for two fluids: 1% and 2% CMC solutions. It shows (i) once again,

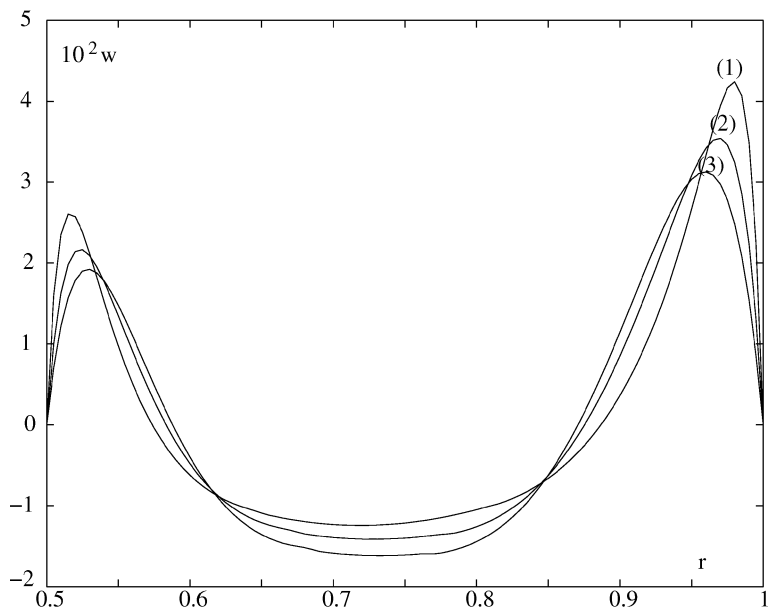

Figure 12. Tangential velocity profiles for $\phi = \pi/2$; $Re = 40$; $n = 0.7$; $Pr = 348.3$; $Gr = 20480$ and $X^+ = 1.08 \cdot 10^{-2}$. Effect of Pearson number: (1) $Pn = 16$; (2) $Pn = 6$; (3)$Pn = 0$.

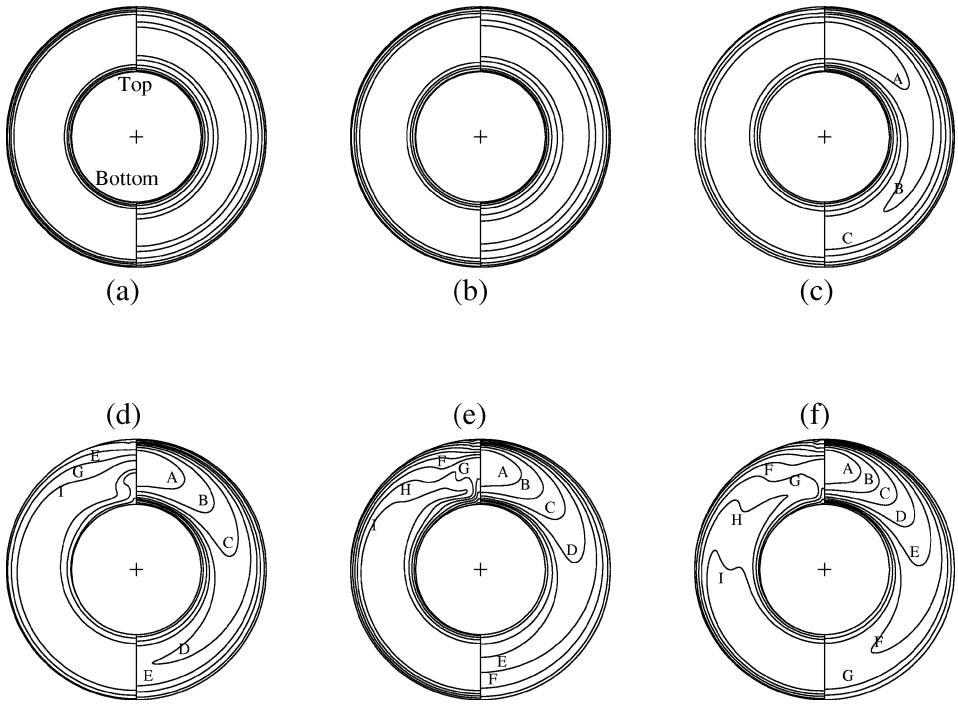

Figure 13. Isovalues of $(T - T_e)/(T_{\max} - T_e)$ at left, and isovalues of $U/U_{\max}$ at right, for $Re = 40$, $Gr = 20480$, $Pr = 348.3$, $Pn = 16$, $n = 0.7$ and $r_1 = 0.5$. Isovalues: $A = 0.9$, $B = 0.8$ then with a step of 0.1 until I = 0.2: (a) $X^+ = 8.97 \cdot 10^{-4}$, four isotherms B, E, G, I and five axial velocity contours H, F, D, B, A from the heated wall to the central zone; (b) $X^+ = 1.8 \cdot 10^{-3}$, four isotherms B, E, G, I and five axial velocity contours H, F, D, B, A, from the heated wall to the central zone; (c) $X^+ = 3.6 \cdot 10^{-3}$ four isotherms B, E, G, I and six axial velocity contours H, F, D, B, A, from the heated wall to the central zone; (d) $X^+ = 7.2 \cdot 10^{-3}$ four isotherms B, E, G, I from the heated wall to the central zone and seven axial velocity contours A, B, C, D, E, F, and H; (e) $X^+ = 1.2 \cdot 10^{-2}$ isotherms A to I from the heated wall to the central zone; (f) $X^+ = 1.8 \cdot 10^{-2}$ isotherms A to I from the heated wall to the central zone.

near the entrance section, the forced convection mechanism is dominant; (ii) the wall temperature difference $[T(\phi = 0) - T(\phi = \pi)]$ increases with x^*. According to Abid et al. [30], beyond a certain axial position, which depends on *Gr*, *Pe* and *Re*, this temperature difference becomes constant, corresponding to the establishment of the thermal field; (iii) for sufficiently important secondary flow intensity, and after the step corresponding to the forced convection dominating mechanism, the temperature $T(\phi = 0)$ evolves very slowly (see *figure 16(b)*). According to Yao [31,32], the downward stream forms a stagnation-like flow locally along the bottom of the outer cylinder wall. The convective effect of this locally stagnant flow prevents the boundary layer from growing. Finally, the ratio $[T_t - T_b]/\Phi^2$, for all the experimental runs, is reported in *figure 15*. The asymptotic solution, given by:

$$[\theta_{\phi=\pi} - \theta_{\phi=0}] \approx 2\varepsilon_1 (ax)^2 \left[\left|G_{10}(0)\right| + \varepsilon_2 (ax)^{1/3} \left|G_{11}(0)\right|\right],$$

is represented by a dashed line. It describes very well the experimental results except for 1% CMC and far from the entrance section. A good agreement is found between the numerical, experimental and asymptotic results in the entrance region. *Figure 16* illustrates the local Nusselt number obtained at $\phi = 0$ and π as a function of X^+. Experimental, numerical and asymptotic results are represented respectively by circle, continuous and dashed lines. For $X^+ \leqslant X_c^+$, the difference between $Nu(\phi = 0)$ and $Nu(\phi = \pi)$ is rather small, since the forced convection is the dominant mechanism. For $X^+ > X_c^+$, this difference is more pronounced indicating the dominant effect of the buoyancy forces.

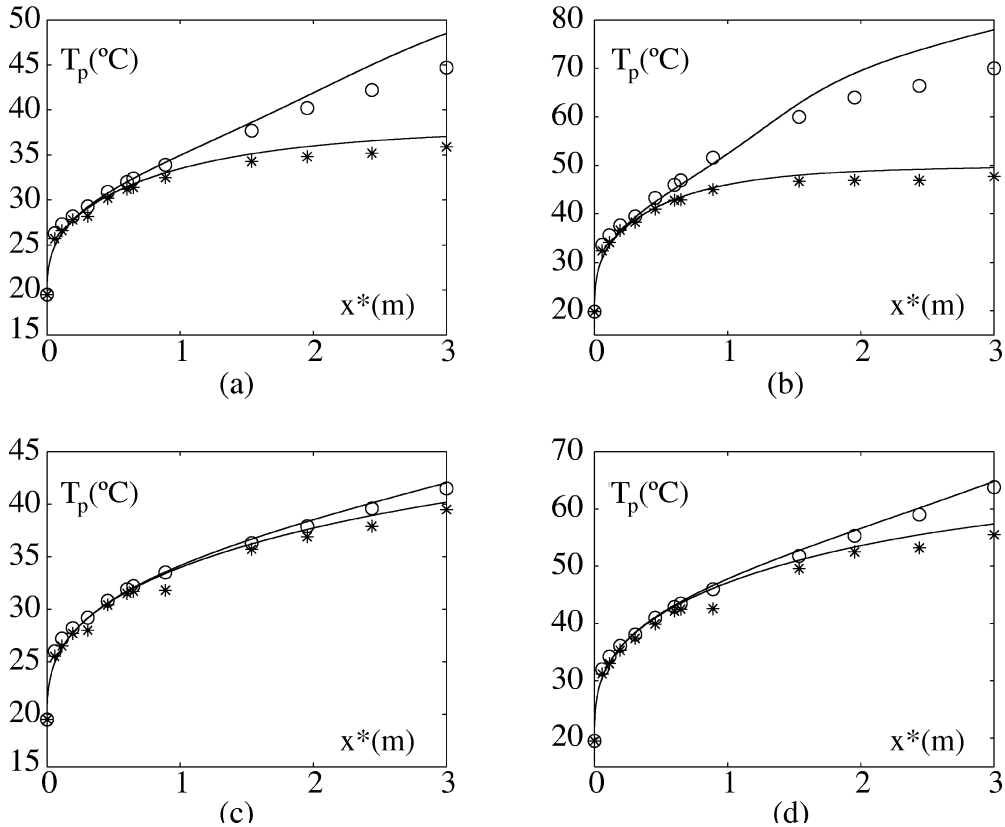

Figure 14. Evolution of the outer cylinder wall temperature at $\phi = 0$ and $\phi = \pi$. Case of 1% CMC solution with $Qv = 1000$ (l/h) and $Te = 19°C$: (a) $\Phi_1 = 3673\ W/m^2$, $\Phi_2 = 3893\ W/m^2$; (b) $\Phi_1 = 7643\ W/m^2$, $\Phi_2 = 8102\ W/m^2$. Case of 2% CMC solution with $Qv = 1300$ (l/h) and $Te = 19°C$; (c) $\Phi_1 = 4053\ W/m^2$, $\Phi_2 = 4296\ W/m^2$; (d) $\Phi_1 = 8346\ W/m^2$, $\Phi_2 = 8775\ W/m^2$. (—) numerical solution.

The thermal stratification described above, combined with the variation of K with T, modify the axial flow behavior. This can be illustrated through the evolution of the axial velocity profil along the heating zone for $\phi = 0$ and $\phi = \pi$ given by *figure 17*.

Near the entrance section the forced convection is dominant. The axial flow is decelerated in the central zone and accelerated near the wall, as shown by curves (1) and (2). Further downstream, the secondary flow increases progressively and leads to the appearance of a low density fluid layer with a higher temperature at the half upper part of the annular duct. The decrease of K with increasing T, induces therefore an acceleration of the axial flow for $\pi/2 \leqslant \phi \leqslant \pi$ and a deceleration for $0 \leqslant \phi \leqslant \pi/2$ as shown in *figures 13(d)–13(f)*. *Figure 17* shows clearly the flow acceleration at $\phi = \pi$ and a deceleration at $\phi = 0$ (see curves 3, 4, 5 and 6). These results are confirmed experimentally. *Figures 18* and *19* show axial velocity profiles measured, before and after heating, at three azimuthal positions ($\phi = 0, \pi/2$ and π). They were obtained for 2% CMC solution, $Qv = (1005 \pm 10)$ l/h; $\phi_1 = 8000\ W/m^2$ and $\phi_2 = 8350\ W/m^2$. Theoretical profiles are presented by continuous lines. Computations take into consideration that velocities were measured 4.5 cm away from the heated zone. A good agreement is obtained between the numerical and experimental results. From this reorganization of the flow observed far from the entrance, these results a decrease of a temperature difference between the upper part and lower part of the duct with increasing *Pn*.

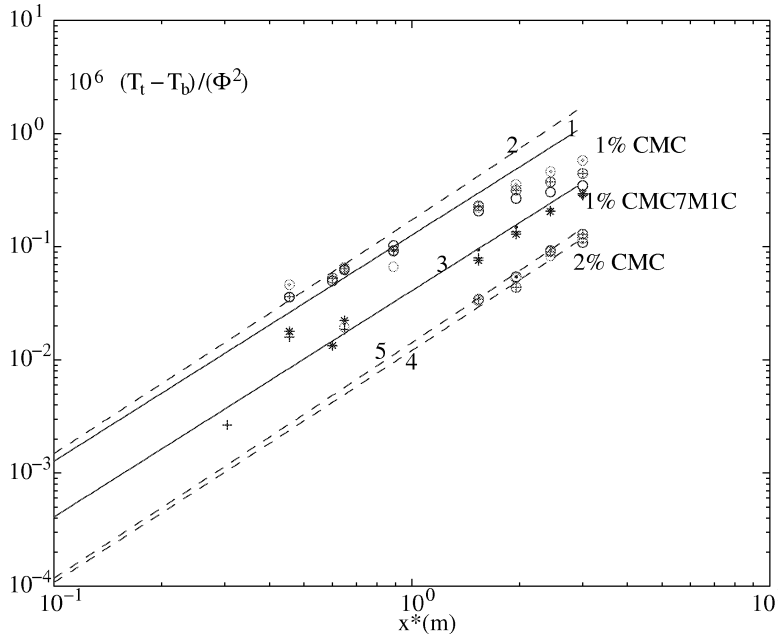

Figure 15. Evolution of the ratio $(T_t - T_b)/\Phi^2$ for outer cylinder, as a function of the axial position. (1) Case of 1% CMC solution: ⊙, $\Phi_1 = 3673\ W/m^2$, $\Phi_2 = 3893\ W/m^2$; ⊕, $\Phi_1 = 5940\ W/m^2$, $\Phi_2 = 6250\ W/m^2$; ∘, $\Phi_1 = 7643\ W/m^2$, $\Phi_2 = 8102\ W/m^2$; curves (1) and (2) are the asymptotic solutions for the highest and the lowest flux. (2) Case of 1% CMC7M1C solution: ∗, $\Phi_1 = 3831\ W/m^2$, $\Phi_2 = 4816\ W/m^2$; +, $\Phi_1 = 5831\ W/m^2$, $\Phi_2 = 6130\ W/m^2$; curve (3) is the asymptotic solution for $Pn = 0$. (3) Case of 2% CMC solution: ⊕, $\Phi_1 = 4053 W/m^2$, $\Phi_2 = 4296\ W/m^2$; ⊙, $\Phi_1 = 8346\ W/m^2$, $\Phi_2 = 8875\ W/m^2$; curves (4) and (5) are the asymptotic solution for the highest and the lowest flux.

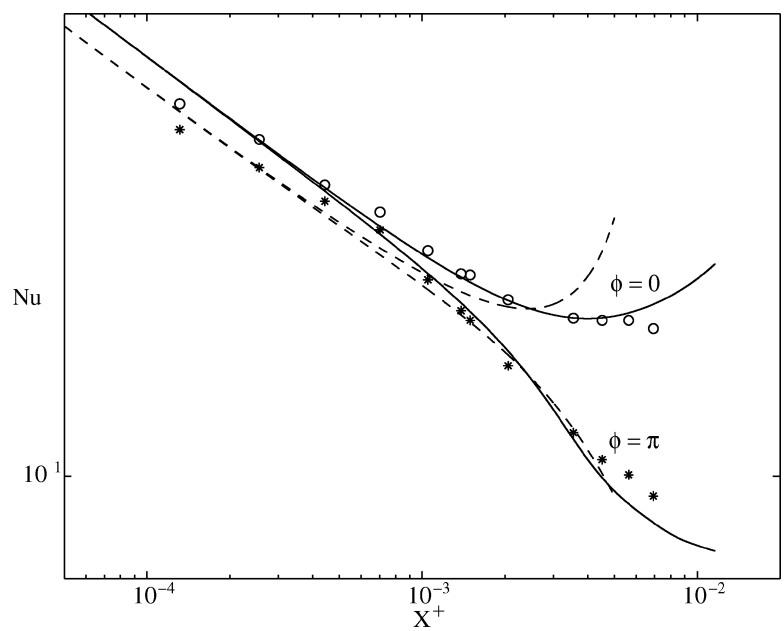

Figure 16. Local Nusselt number at $\phi = \pi$ and $\phi = 0$ along the heating zone for 1% CMC solution, $n = 0.9$, $b = 0.03°C^{-1}$, $\Phi_1 = 7640\ W/m^2$, $\Phi_2 = 8100\ W/m^2$ and $Qv = 1050$ (l/h). $Re = 99$, $Gr = 9645$ and $Pr = 251$. (- - -) asymptotic solution; (—) numerical solution; (∘), (∗) experimental results.

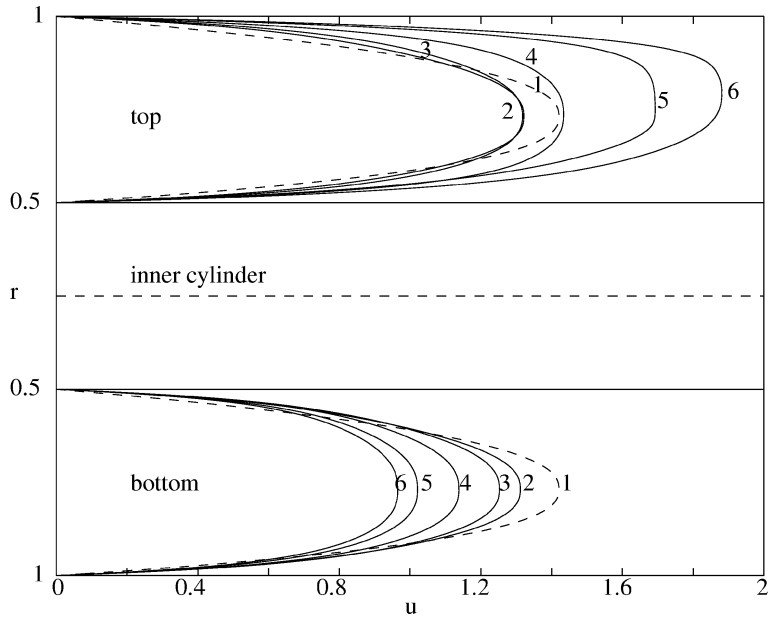

Figure 17. Evolution of the axial velocity profile along the heating zone for $Re = 40$, $Pr = 348.3$, $Gr = 20240$ and $Pn = 8$: (1) $X^+ = 0$; (2) $X^+ = 9.0 \cdot 10^{-4}$; (3) $X^+ = 1.8 \cdot 10^{-3}$; (4) $X^+ = 3.6 \cdot 10^{-3}$; (5) $X^+ = 7.2 \cdot 10^{-3}$; (6) $X^+ = 1.1 \cdot 10^{-2}$.

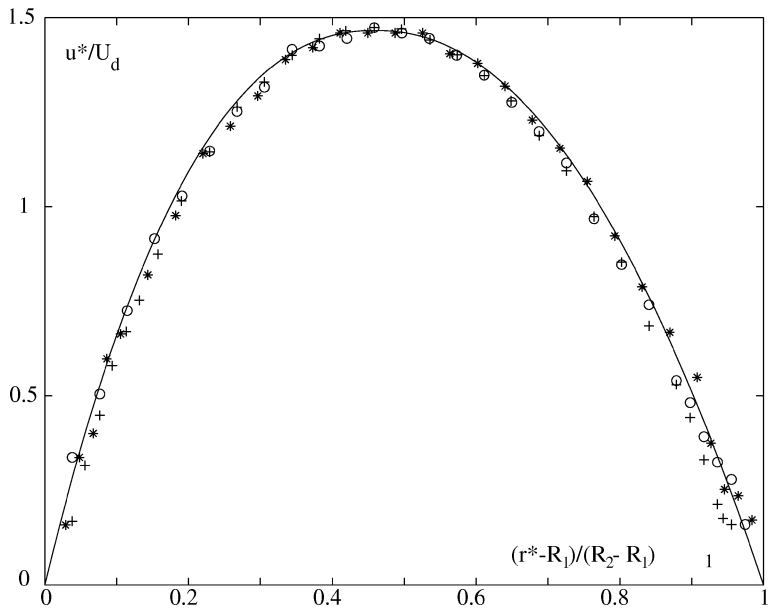

Figure 18. Isothermal axial velocity profiles at different azimuthal positions in the case of 2% CMC solution: $n = 0.83$ and $Qv = 1005$ (l/h): ($\circ$)$\phi = 0$; (+) $\phi = \pi/2$; ($*$) $\phi = \pi$; (—-) theoretical profile.

Concerning the pressure drop $[P]_{X_f}^0$ along the heating zone, measurements were performed, for 1% CMC and 2% CMC solutions, and various Φ: $0 \leqslant \Phi \leqslant 10^4$ W/m^2. The results are in very good agreement with the numerical calculation and indicate an exponential decrease with Φ. It seems that the secondary flow has a weak effect on $[P]_{X_f}^0$.

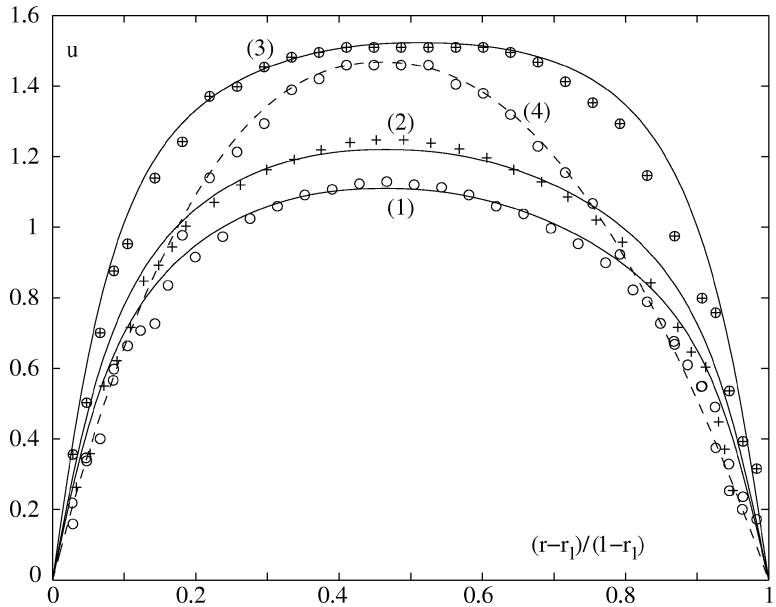

Figure 19. Axial velocity profiles at the exit of the heating zone and at different azimuthal positions. Case of 2% CMC solution with $n = 0.83$, $K = 0.74\exp(-0.039T)$, $Te = 19°\mathrm{C}$, $Qv = 1005$ (l/h), $\Phi_1 = 8000\ W/\mathrm{m}^2$ and $\Phi_2 = 8350\ W/\mathrm{m}^2$. (1) $\phi = 0$; (2) $\phi = \pi/2$; (3) $\phi = \pi$; (4) isothermal profile; (—) numerical solution.

7. Conclusion

Laminar mixed convection in a horizontal annular duct for power law fluids with variable consistency has been analyzed experimentally and numerically. For large Péclet numbers, an asymptotic solution was derived. The results obtained show that:

(1) In the case of forced convection, the decrease of K as T increases induces a radial motion of fluid particles towards the heated walls. In the boundary layer, the flow is quickly accelerated very near the inlet section, then the acceleration declines as $(ax)^{-1/3}$. The opposite phenomenon is observed in the core region. An analytical expression of the local Nusselt number is deduced from the asymptotic solution. It indicates that in the thermal entrance region, the enhancement of the Nusselt number due to the decrease of K near the heated walls, is more important as the shear thinning of the fluid increases.

(2) In the case of mixed convection with constant consistency, the secondary flow starts from the entrance section. Its intensity increases linearly along the heating zone, as $\varepsilon_1(ax)$, reaches a maximum, and decreases slightly towards an asymptotic value corresponding to the fully developed dynamic regime. The axial flow is accelerated like (ax) in the lower part of the duct, and decelerated in the upper part with the same rate. This secondary flow leads to a thermal stratification. The dimensionless temperature difference $(\theta_t - \theta_b)$ between the top and the bottom of the duct, evolves near the entrance as $\varepsilon_1(ax)^2$. However, the forced convection remains the dominant mechanism in the heat transfer until a dimensionless axial position X_c^+. Beyond, X_c^+ the natural convection becomes the dominant mechanism. The dimensionless axial position X_c^+, where the two mechanisms are of the same order, is determined from scaling analysis. It depends on the flow behavior index as: $X^+_{c,nnewt}/X^+_{c,newt} = 1/\Pi$.

(3) In the situation of mixed convection with variable consistency, the decrease of K as T increases, reduces X_c^+ and leads to an increase of the circulation intensity I_{sf}. In the entrance region, $I_{sf,th} - I_{sf,nth}$ varies as $\varepsilon_1\varepsilon_2(ax)^{4/3}$. The temperature difference $(\theta_t - \theta_b)$ increases near the entrance. Far from the entrance, the

combined effects of thermal stratification and the decrease of $K(T)$ lead to an acceleration of the fluid at the upper part of the annular duct, which in turn reduces the difference $(\theta_t - \theta_b)$.

Appendix

Table AI. Values of $F''_{10}(0)$, $H''_{10}(0)$, $-10^2 \times G_{10}(0)$, $H''_{01}(0)$ and $-G_{01}(0)$ for radius ratio of 0.5 and various values of n and Pr.

n	Pr	$F''_{10}(0)$	$H''_{10}(0)$	$-10^2 \times G_{10}(0)$	$H''_{01}(0)$	$-G_{01}(0)$
1	10	0.25022	0.03429	0.26672	7.03608	0.10581
	50	0.28078	0.02578	0.20855	7.62924	0.11828
	100	0.29043	0.02205	0.18162	7.77436	0.12136
	250	0.30050	0.01753	0.14853	7.89933	0.12401
	500	0.30640	0.01449	0.12611	7.95962	0.12530
0.8	10	0.25022	0.04009	0.29130	9.23482	0.12979
	50	0.28078	0.03036	0.22886	10.10541	0.146301
	100	0.29043	0.02603	0.19935	10.32257	0.15061
	250	0.30050	0.02074	0.16282	10.51111	0.15436
	500	0.30640	0.01719	0.13805	10.60210	0.15617
0.5	10	0.25022	0.05719	0.34952	16.89502	0.19507
	50	0.28078	0.04407	0.27820	18.89421	0.22791
	100	0.29043	0.03799	0.24285	19.41568	0.23656
	250	0.30050	0.03046	0.19823	19.87784	0.24428
	500	0.30640	0.02536	0.16767	20.10304	0.24803

Acknowledgments

The authors would like to thank Professor J.P. Brancher for fruitful discussions. Thanks are also due to the anonymous reviewers for their comments, useful in improving this work.

References

[1] Morton B.R., Laminar convection in uniformly heated horizontal pipes at low Rayleigh numbers, Q. J. Mech. Appl. Math. 12 (1959) 410–420.
[2] Mojtabi A., Caltagirone J.P., Analyse du transfert de chaleur en convection mixte laminaire entre deux cylindres coaxiaux horizontaux, Int. J. Heat Mass Tran. 28 (1980) 1369–1375.
[3] Kotake S., Hattori N., Combined forced and free convection heat transfer for fully developed laminar flow in horizontal annuli, Int. J. Heat Mass Tran. 28 (1985) 2113–2120.
[4] Terhmina O., Mojtabi A., Roux B., A numerical procedure for three-dimensional mixed convection developing flow in an axisymmetric geometry, Eur. J. Mech. B-Fluids 1 (1992) 21–38.
[5] Nonino C., Del Giudice S., Finite element analysis of laminar mixed convection in the entrance region of horizontal annular ducts, Numer. Heat Tr. A-Appl. 29 (1996) 313–330.
[6] Lundberg R.E., McCuen P.A., Reynolds W.C., Heat transfer in annular passages. Hydrodynamically developed flow with arbitrarily prescribed wall temperatures or heat fluxes, Int. J. Heat Mass Tran. 6 (1963) 495–529.
[7] Tiu C., Bhattacharya S., Developing and fully developed velocity profiles for inelastics power law fluids in an annulus, AICHE J. 20 (1974) 1140–1148.
[8] Shah R.K., London A.L., Advances in Heat Transfer, Vol. 1, Academic Press, New York, 1978.

[9] Gray D.D., Giorgini A., The validity of the Boussinesq approximation for liquid and gases, Int. J. Heat Mass Tran. 19 (1975) 545–551.
[10] Choudhury D., Patankar S.V., Combined forced and free laminar convection in the entrance region of an inclined isothermal tube, J. Heat Tran. 110 (1988) 901–908.
[11] Bird R.B., Armstrong R.C., Hassager O., Dynamics of Polymeric Liquids, Vol. 1, Wiley, New York, 1987.
[12] Patankar S.V., Numerical Heat Transfer and Fluid Flow, McGraw-Hill, New York, 1980.
[13] Ogawa M., Schubert G., Zebib A., Numerical simulation of three-dimensional thermal convection in a fluid with strongly temperature-dependent viscosity, J. Fluid Mech. 233 (1991) 298–328.
[14] Briley W.R., Numerical method for predicting three dimensional steady viscous flow in ducts, J. Comp. Phys. 14 (1974) 8–28.
[15] Fletcher C.A.J., Computational for Fluid Dynamics, Springer-Verlag, New York, 1992.
[16] Worsoe-Schmidt A.E., Heat transfer in the thermal entrance region of circular tubes and annular passages with fully developed laminar flow, Int. J. Heat Mass Tran. 10 (1967) 541–545.
[17] Tanaka M., Mitsuichi N., Non-Newtonian laminar heat transfer in concentric annuli, Kagaku Kogaku 38 (1974) 664–671.
[18] van Dyke M., Perturbation Methods in Fluid Mechanics, Academic Press, New York, 1964.
[19] Acrivos A., Goddard J.D., Asymptotic expansions for laminar forced convection heat and Mass Transfer. Part 1. Low speeds flows, J. Fluid. Mech. 23 (1965) 273–291.
[20] Acrivos A., On the combined forced and free convection heat transfer in laminar boundary layer flows, Chem. Eng. Sci. 21 (1965) 343–352.
[21] Bejan A., Convection heat transfer, Willey, New York, 1984.
[22] Nouar C., Deasubry C., Zenaidi H., Numerical and experimental investigation of thermal convection for a thermodependent Herschel-Bulkley fluid in an annular duct with rotating inner cylinder, Eur. J. Mech. B-Fluids 17 (1998) 1–26.
[23] Ockendon H., Ockendon J.R., Variable viscosity flows in heated and cooled channels, J. Fluid. Mech. 83 (1977) 177–190.
[24] Richardson S.M., Flow of variable viscosity fluids in ducts with heated walls, J. Non-Newton. Fluid 25 (1986) 137–156.
[25] Xin S., Le Quere P., Daube O., Natural convection in a differentially heated horizontal cylinders: Effects of Prandtl number on flow structure and instability, Phys. Fluids A 9 (4) (1997) 1014–1033.
[26] Mizushina T., Ito R., Kuriwake Y., Yahikazawa K., Boundary layer heat transfer in a circular tube to Newtonian and non-Newtonian fluids, Kagaku Kogaku 31 (1967) 250–255.
[27] Joshi S., Bergles A.E., Experimental study of laminar heat transfer to in-tube flow of non-Newtonian fluids, J. Heat Trans-T. ASME 102 (1980) 397–401.
[28] Hong S.W., Bergles A.E., Theoretical solutions for combined forced and free convection in horizontal tubes with temperature- dependent viscosity, J. Heat Tran. 98 (8) (1976) 459–465.
[29] Orfi J., Galanis N., Nguyen C.T., Développement simultané hydrodynamique et thermique d'un écoulement laminaire dans un tube incliné en regime de convection mixte, Rev. Gen. Therm 36 (1997) 83–92.
[30] Abid C., Papini F., Ropke A., Veyret D., Étude de la convection mixte dans un conduit cylindrique. Approches analytique/numerique et détermination expérimentale de la température de paroi par thermographie infrarouge, Int. J. Heat Mass Tran. 32 (1994) 91–101.
[31] Yao L.S., Free forced convection in the entry region of a heated straight pipe, J. Heat Trans-T. ASME 100 (5) (1978) 212–219.
[32] Yao L.S., Entry flow in a heated straight tube, J. Fluid. Mech 3 (1978) 465–483.